The Pennsylvania State University

The Graduate School

DEVELOPMENT OF A COMPUTATIONAL MODEL OF A HIGH TEMPERATURE LITHIUM-CARBON DIOXIDE REACTOR FOR SPACE POWER GENERATION

A Thesis in

Mechanical Engineering

by

Eric A. Moser

Submitted in Partial Fulfillment
of the Requirements
for the Degree of

Master of Science

August 2022

The thesis of Eric A. Moser was reviewed and approved by the following:

Alexander S. Rattner
Associate Professor of Mechanical Engineering
Thesis Co-Advisor

Joseph J. Cor
Assistant Research Professor of Mechanical Engineering
Thesis Co-Advisor

Daniel J. Leonard
Assistant Research Professor – Applied Research Laboratory

Michael P. Manahan
Assistant Research Professor of Mechanical Engineering

Daniel C. Haworth
Professor of Mechanical Engineering
Head of the Department of Mechanical Engineering

ABSTRACT

There are significant challenges in powering a planetary lander mission to Venus due to its extreme temperatures. A planetary lander will require a refrigeration system to keep cool which requires a power system that can generate enough power for this purpose. A reaction that uses lithium metal and the in-situ carbon dioxide from the Venus atmosphere offers a promising solution to this power requirement.

Previously, experimental tests have been conducted at various lithium bath temperatures, mass flow rates, and reactor geometries, to determine the thermal energy output of this reaction. The overall energy output is unknown because the specific energy produced from this reaction will be lower than theory due to issues such as crusting which could prematurely end the reaction. The purpose of this thesis is to create a computational fluid dynamics (CFD) model of previously-completed experimental tests that includes the reaction between lithium and carbon dioxide. This CFD model is being developed as part of the development process of a tool for analyzing the performance of a stored chemical energy propulsion system (SCEPS) combustor. The goal of this experimentally-developed model is to help guide SCEPS designs and gain insight into the operation of SCEPS combustors.

It is currently unknown why some experimental reactors experienced crusting that prematurely ended the combustion inside the reactor and why some reactors did not. Accordingly, the CFD model developed here has been exercised in a simplified configuration to explore this crusting phenomenon in greater detail.

The CFD model is compared against experimental results for product yield, mass flow rate, and overall degree of completion of the reaction. The product yield of the simulated reaction is similar to experimental results. Likewise, the degree of completion correlates well to the experimental results and to theory. A similar utilization rate of lithium was achieved in the baseline model upon comparison to the experimental results. Additionally, simulations exploring crust formation may point to ways to study this phenomenon computationally.

Further research should be conducted into the model that experienced crust formation to better understand the mechanisms that caused the crust formation to occur. This crust formation is important to understand so that future reactors can be operated in such a way that all the energy available in this reaction can be accessed without being limited by a crust of products prematurely ending the reaction. These additions to the model could contribute to making it a tool for reactor design.

TABLE OF CONTENTS

LIST OF FIGURES

LIST OF TABLES

NOMENCLATURE

C_p	Specific Heat Capacity [J/kg-K]
CM	Created Mass [kg]
f	Degree of Completion [-]
H	Heat of Reaction on Mass Basis [J/kg]
h_f	Enthalpy of Formation [J/kg]
i	Particular Species of Interest [-]
L	Liquid Volume Fraction [-]
M	Mass [kg]
MW	Molecular Weight [kg/kmol]
N	Number of Kilomoles [kmol]
P	Pressure [Pa]
Q	Heat of Reaction on Volume Basis [J/m^3]
R	Reaction [kh/m^3-s]
RoC	Rate of Change [-]
S	Solid Volume Fraction [-]
SLM	Standard Liters per Minute [L/min]
T	Temperature [K]
t	time [s]
u	velocity [m/s]
V	Volume [m^3]
Y	Mass Fraction [-]
ρ	Density [kg/m^3]
χ	Volume Fraction [-]

ACKNOWLEDGEMENTS

I would like to thank my advisors Dr. Alexander Rattner and Dr. Joseph Cor. Without their help, this final thesis would not have been possible. Through their time and patience, I have learned far more than I could ever have hoped. I have had a wonderful time working on this complex research problem with them.

I would also like to thank Dr. Daniel Leonard who provided valuable feedback in both modeling this complex issue and reviewing this thesis. Likewise, I would like to thank Dr. Michael Manahan who provided valuable feedback which increased the final quality of this thesis.

Chapter 1

Introduction

Venus is of particular importance to study because analyzing the planet's formation and transformation could help researchers understand more about Earth and the other terrestrial planets [1]. Venus, often called "Earth's twin," was formed in a similar way to the Earth and has similar size, mass, density, and surface composition to Earth. However, Venus possesses an extreme environment due to unknown factors. For example, it is unknown how the planet's atmosphere evolved over time, whether Venus ever had oceans, when and why the runaway greenhouse effect began, and how Venus loses heat. These unknown factors have contributed to an environment that is radically different from Earth despite the similarities Venus has to Earth.

Venus has an extreme environment where the temperature and pressure at the surface are approximately 460°C and 93 bar, respectively. This environment causes Venus to be a challenging planet to explore. Consequently, relatively little is known about Venus. To advance knowledge about Venus, future missions to explore our planetary neighbor are being conceived. For example, currently proposed missions to Venus include a sample return mission [2] and a Venus rover mission [3]. These missions seek to build upon what was discovered by the earlier missions to Venus. The early notable missions to study Venus were the Venera missions which included probes, landers, balloons, and orbiters [4]. Venera 13 survived on Venus for approximately two hours and is recorded as the longest duration surface mission on the planet. While these

short missions are notable accomplishments, longer-lived missions are necessary to collect more data on Venus.

A stored chemical energy propulsion system (SCEPS) concept was proposed to power a longer-lived Venus mission because of the higher specific energy that the lithium-carbon dioxide reaction offers compared to batteries. This reaction produces enough power to provide active cooling in addition to power generation, while conventional batteries cannot. To aid in these exploratory efforts, a SCEPS system has been experimentally tested to determine the energy output that is achievable from this system for a future Venus mission. Carbon dioxide (CO_2) has been chosen as the oxidizer because of its abundance in the atmosphere of Venus, allowing for the SCEPS reactor to use in-situ CO_2 instead of carrying the oxidizer from Earth, lowering the overall weight of the system. A SCEPS system is being developed because it offers an energy pathway to power missions to Venus that would otherwise be too costly for other power generation options.

A SCEPS system is a constant volume system that does not need to exhaust to the atmosphere. It is a system that contains a metal fuel that is melted into a molten state and reacted with a gaseous oxidizer. This reaction produces products that are denser than the reactants and so the products should sink to the bottom of the reactor. Because this reaction is exothermic, the heat generated can be transported via heat pipes into a Stirling engine for power generation. This power is enough to provide the lander with refrigeration as well as provide power to the equipment onboard the lander. A schematic of a Li-CO2 SCEPS reactor (personal communication with Dr. Alexander Rattner) is provided in Figure 1.

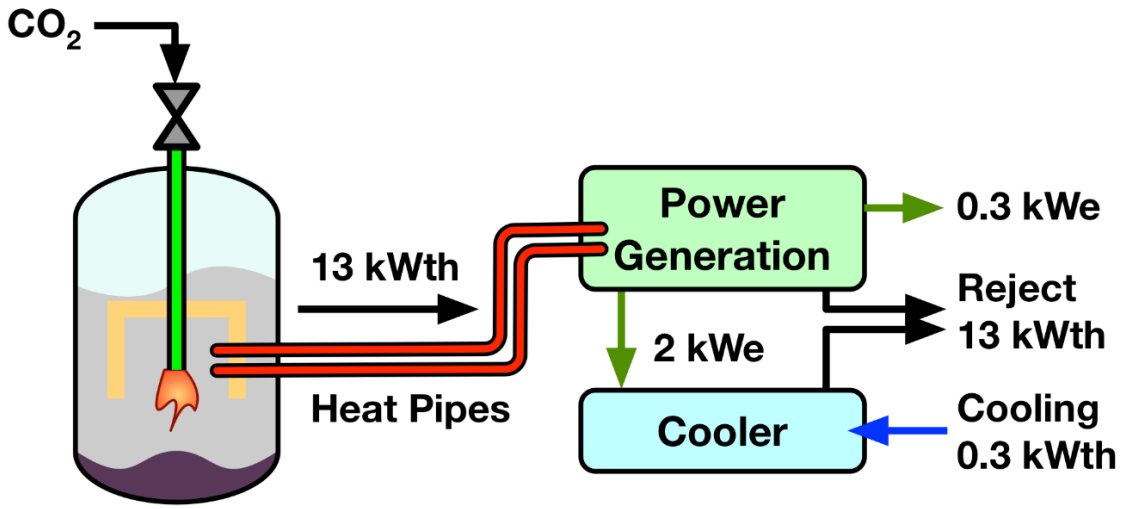

Figure 1: Schematic of a Li-CO_2 SCEPS reactor

Greer et al. [5] experimentally evaluated five different SCEPS reactors that varied in reactor temperature, heat delivery mechanisms, and wicking systems for lithium (Li) fuel with CO_2 oxidizer. From these experiments, the mass flow, temperature, and pressure during testing were measured, and computed tomography (CT) scans after testing were conducted to estimate the degree of product formation.

In this study, the Reactor 3.0 and Reactor 3.2 designs of the five experimental tests in the Greer et al. [5] paper will be replicated through the creation of a computational fluid dynamics (CFD) model. A CFD analysis of these reactors is sought so that further understanding of the reaction mechanisms inside these reactors could be more fully understood. A CFD model will help aid the design and development of Li-CO_2 SCEPS reactors so that a new power generation option is available for planetary lander missions.

Chapter 2

Literature Review

2.1. Motivation for research

Furthering our knowledge about Venus will help us to better understand Earth. Recently, scientists and researchers have renewed their interest in longer duration missions to Venus to build upon the knowledge gained from previous short-lived missions to Venus. However, generating power for these expanded Venus missions remains a challenge.

Powering a Venus-related mission remains a challenge due to the planet's extreme heat, pressure, and cloud cover. Currently, batteries are being developed that can operate in the ambient temperature of Venus and utilize the in-situ CO_2 in the Venus atmosphere [6]. Solar cells that can operate in the cloudy environment and extreme heat of Venus [7] are also being devised. Additionally, missions using radioisotope derived power remain a possibility. However, there are drawbacks to these technologies. The battery concept described above is still in development although sodium-sulfur (NaS) batteries are a proven viable alternative, and the solar cell concept will suffer from the low light levels and high temperatures on Venus. The radioisotope-powered missions have been proven successful by numerous other missions in outer space and could power a cooling system [3, 8] to shield against the heat of the Venus environment. However,

this technology remains prohibitively expensive and is relatively inefficient at power conversion with an efficiency of 23.4% [3, 9].

A planetary decadal survey by the National Research Council [10] outlined the scientific value of Venus as a future target for an in-situ explorer mission. The Concurrent Multidisciplinary Preliminary Assessment of Space Systems (COMPASS) team from NASA created a technical report for a long-life lander to investigate the Venus environment [11]. The objective of this mission is to further study Venus by landing a spacecraft on its surface that can generate power through the combustion of lithium and carbon dioxide. Accordingly, Greer et al. [5] has undertaken testing of multiple experimental reactors in different configurations and bath temperatures to support further understanding of the reaction parameters of the lithium and carbon dioxide reaction. These experimental tests used approximately 200 g of lithium and produced an effective fuel specific energy of 25.6 MJ/kg_{Li} for their Reactor 3.2 design. This combustion process could be used to heat a duplex Stirling engine to power and cool the lander until the lithium fuel is exhausted.

2.2. Benefits of Li-CO_2 power generation

A lithium carbon dioxide combustion reaction is an alternative to well-established power sources for space applications because this process is capable of generating enough power to operate a Venus lander for a few days through the use of a Stirling engine. Miller et al. [12] outlined the feasibility of the Li-CO_2 power generation for a

Venus mission. The reaction between Li-CO_2 is described through a multistep reaction consisting of three reactions:

$$5Li + CO_2 \rightarrow 2Li_2O + 0.5\,Li_2C_2 \quad (1)$$

$$2Li_2C_2 + 3CO_2 \rightarrow 2Li_2CO_3 + 5C \quad (2)$$

$$Li_2O + CO_2 \leftrightarrow Li_2CO_3 \quad (3)$$

Once the initial Li-CO_2 reaction from equation (1) has commenced, and enough lithium carbide (Li_2C_2) and lithium oxide (Li_2O) are present, the lithium carbide and lithium oxide can begin to react with CO_2. Lithium carbide can react with CO_2 in equation (2) to produce lithium carbonate (Li_2CO_3) and carbon, and lithium oxide can react with CO_2 in equation (3) to form lithium carbonate. However, at temperatures above 800°C, equation (3) moves in the reverse direction, disassociating Li_2CO_3 back into Li_2O and CO_2. From this multistep reaction, and without Li_2CO_3 disassociating, an available 28.6 MJ/kg of lithium fuel from the entire set of reactions could be achieved. On a CO_2 mass basis, the specific energy for the first reaction is approximately 18.9 MJ/kg_{CO2}. The second and third reactions have specific energies of 8.6 MJ/kg_{CO2} and 5.1 MJ/kg_{CO2}, respectively [5].

An estimated system specific energy for this set of reactions is 1.1 kW-hr/kg_{Li} using in-situ CO_2 [12] with a system energy density of 650 kW-hr/m^3. The system specific energy noted by Miller et al. [12] assumes that there is some amount of electrical conversion efficiency. In comparison, a NaS battery operating at 500°C has a system specific energy of 0.3 kW-hr/kg with a system energy density of 350 kW-hr/m^3 [12].

Greer et al. [13] argued that a short-duration mission to Venus would benefit from a SCEPS reactor due to cost constraints, mass constraints, and solar constraints of other

power generation options. As an example, for a five-day Venus mission, a 400 kg NaS battery mass would be required to produce 1kW. If the mission were to be extended to ten days, the same power output could be achieved using a lithium fuel mass of 172 kg [13]. A surface mission that requires the 1kW of power described above is not feasible when powered by photovoltaic cells. At the surface of Venus, only about 8.7 W/m^2 of solar power is obtainable [7], so impractically large solar panels would need to be brought from earth to obtain the same power output. Furthermore, the cost of the mission is intended to be either a Discovery ($500M) or New Frontiers ($750M to $780M) class mission [11], where the inclusion of a plutonium powered rover may be cost prohibitive.

Further, when considering that the products of the Li-CO_2 reaction are denser than the lithium [13], all the reactants and products can remain inside the reactor which removes a requirement to exhaust the products to the atmosphere which is typically needed for conventional combustion processes.

The combustion of lithium and carbon dioxide is an exothermic reaction that generates enough heat to act as a power source. It is well known that molten lithium is highly reactive with many gases, and to further understand lithium reactivity, the combustion of lithium with different oxidizers has been examined [14]. During these lithium-oxidizer studies, it was determined that the maximum consumption rate of lithium in the Li-CO_2 reaction was 994 mol/m^2-min [14] under a pressure of 0.18 atm and at a temperature of 540°C, which is useful for further understanding the rate at which lithium combusts, releases heat, and forms intermediate products. Yuasa et al. [15] determined that the ignition process of the Li-CO_2 reaction first occurred in the vapor phase and then progressed to a surface reaction. This process should be noted because it

indicates that lithium gas combustion plays a role in product formation and heat generation before the reaction progresses to the desired surface reaction where the bulk of the products and heat can be generated.

The reaction between Li-CO_2 for use on other planets was investigated over the years. An experiment conducted in the late 1960's investigated different fuel-oxidizer combinations in a simulated Venus atmosphere [16] and found that the combustion of lithium and beryllium emitted sufficient heat to be a feasible power source for a Venus application. More recently, Miller et al. [12] and Baker et al. [17] discussed the potential for using a SCEPS reaction of Li-CO_2 for generating power on Venus using in-situ CO_2 in the Venus atmosphere. Greer et al. [5, 13] conducted experiments for the Li-CO_2 reaction which sought to identify the fuel specific energy and operating temperatures of different SCEPS reactor configurations. They reported that at lower reactor temperatures a product crust formed over the lithium bath, limiting fuel utilization, but at higher reactor temperatures nearly all lithium fuel was reacted, which yielded a fuel specific energy of 25.6 MJ/kg of lithium. This suggests that a higher bath temperature is required to react all the available lithium so that an optimal amount of energy can be generated. This finding is important because if the theoretical yield can be achieved, less lithium will need to be brought on the mission, which therefore reduces the overall weight of the reactor.

2.3. Lithium combustion possibilities in power plants

Investigations into the Li-CO_2 reaction for applicability in environmentally friendly power plants as a source for power generation was conducted by Fischer et al. [18] and expanded upon by Schiemann et al. [19, 20]. From this research, it was identified that a closed-loop energy storage process is feasible. Elemental lithium has a high energy storage capacity and can be easily transported as a solid. The lithium could be reacted using an oxidizer that contains the exhaust gasses of existing power plants thereby producing energy as the lithium combusts. The reaction products, which are solids, can then be retransformed into elemental lithium through an electrolysis process using renewable energy sources when power demand is low [19, 20].

These experiments have been conducted under the knowledge that the specific energy of elemental lithium is high. Lithium has the third highest specific energy of all metals/metalloids per mass [20] which leads to relatively high energy output for a relatively low lithium mass requirement. Schiemann et al. [19] determined that with just 256 g of lithium reacting with CO_2, 10 MJ of energy can be generated. Fischer et al. [18] found that 10 MJ of energy could be generated at ambient conditions from 480 cm^3 of lithium if reacted with CO_2. Even on a particle level, these experiments have demonstrated that the Li-CO_2 reaction is a viable way to produce energy from relatively low mass requirements. These low mass requirements and high specific energy of lithium translate into increased viability for this reaction in space applications due to a reduced cost associated with launching this power generation unit into space.

The investigations into renewable energy power plants using lithium fuel provides a further reason to develop a Li-CO_2 reactor model. Understanding these power plant concepts and how they utilize lithium combustion may be helpful in larger scale combustion utilizing a molten lithium bath to further advance power generation concepts for planetary landers. Research findings extend our collective knowledge in lithium combustion which allows for the generation of new planetary lander concepts that build upon this knowledge. Further clarification of how lithium reacts during combustion may further our knowledge of lithium vapor combustion and therefore help increase the lifespan of SCEPS reactors by possibly reducing the rate at which clogs or corrosion may occur.

2.4. Current gap in literature

Although experiments of the SCEPS Li-CO_2 combustion reaction have been conducted, no CFD analysis of the SCEPS Li-CO_2 reaction has been completed to replicate these tests. Some CFD analyses have been completed for the Li-CO_2 reaction [21, 22] and for the Li-SF_6 reaction [23], but not specifically for a Li-CO_2 reactor.

These ideas can be applied to the Li-CO_2 combustion reaction in a SCEPS reactor so that further analysis in CFD can be completed to investigate this reaction more thoroughly for power generation for space applications. Greer et al. [5] described five experimental tests conducted for the Li-CO_2 reaction where a CFD model can be created that can use the presented results as validation for the simulation. The work by Greer et

al. provides a strong foundation to develop and validate a CFD model for the SCEPS system.

It is necessary to understand the physics inside a SCEPS system to create better designed reactors that create heat outputs closer to theoretical limits. In order to do so, a computational approach needs to be taken to better understand the physics involved in these reactors that dictate the mass flow rate, heat output, and overall product generation. Therefore, a CFD model is required to develop the methodology that experimental reactor testing can use to create more successful SCEPS systems.

This thesis therefore presents a CFD model based upon the experimental reactor designs created by Greer et al. [5] for the SCEPS system. This CFD model is intended to predict performance parameters from the combustion of lithium and carbon dioxide through the yield of products and heat transfer. This work is the start of a process of creating a validated CFD model that could be used as a design guide that can help predict trends and evaluate alternative designs prior to building a reactor.

Chapter 3

Methods

3.1. Governing equations

Throughout the modeling process that will be described shortly, the governing equations that describe the fluid flow are the following:

$$\int_V \frac{\partial \rho}{\partial t}\, dV + \int_A \rho u \cdot dA = \int_V S\, dV \tag{4}$$

$$\int_V \frac{\partial \rho u}{\partial t}\, dV + \int_A \rho u (u \cdot dA) = -\int_A P dA + \int_A \tau \cdot dA + \int_V \rho f dV + \int_V S\, dV \tag{5}$$

$$\int_V \frac{\partial \rho E}{\partial t}\, dV + \int_A \rho E (u \cdot dA) = \int_A [(-PI + \tau) \cdot u] \cdot dA + \int_A [k \nabla T] \cdot dA + \int_V (\rho f \cdot u) dA + \int_V \rho \dot{q} dV + \int_V S\, dV \tag{6}$$

where S represents any other source terms not explicitly stated that would be applicable for the governing equations of this model.

Described in equations (4) to (6) are the fundamental governing equations for the conservation of mass, momentum, and energy, respectively. The mass conservation equation (equation 4) ensures mass is conserved through observing the change of mass within a control volume and the net efflux of mass from the control volume. Likewise, momentum is conserved in the model though equation (5). The momentum equation ensues momentum is conserved through observing the rate of change of momentum within the control volume, the net efflux of momentum from the control volume, as well

as the net forces acting on the control volume. Finally, the energy equation (equation 6) ensures energy is conserved through observing the rate of change of energy within the control volume, the net efflux of energy from the control volume, and the rates of viscous work, body work, and heat addition to the control volume.

3.2. Physical model

In order to model the lithium combustion from prior experimental work done by Greer et al. [5], the CFD program, Star-CCM+ by Siemens [24], was chosen. This software package was chosen because of its ability to build representative geometries, meshing, and multiphysics simulations into one package. Star-CCM+ was run on a desktop computer with an Intel Xenon W-2133 processor with 32 gigabytes of memory. A typical simulation of the model took approximately 1.25 hours of physical time and approximately 1.5 weeks of wall time to simulate.

To accurately create the CFD model, accurate dimensions, flow rates, pressures, and temperatures that are representative of the experimental setup needed to be identified and incorporated. Within the architecture of Star-CCM+, a model was built to simulate the combustion of molten lithium with carbon dioxide to generate heat inside a reactor, where the heat is extracted from the system to be used in power generation. Both the combustor that contains the molten lithium and the solid walls of the reactor were simulated inside the model. The combustor interior uses a multiphase material, which allows for more than one distinct compound to exist in the molten lithium bath, and the solid material region is essentially a finite volume thermal model to predict temperature

gradients along the wall. The simulation also uses the axisymmetric model and implicit unsteady time stepping.

The solid material region (i.e., the combustor wall) was simulated using the models of segregated solid energy for energy conservation, and constant density was assumed. The multiphase material physics of the molten combustor interior uses the Volume of Fluid (VOF) multiphase model with a turbulent viscous regime [25], and the k-Epsilon Reynolds-Averaged Turbulence model [26]. The model also includes gravity, segregated multiphase temperature, and average mushy-zone permeability.

The VOF multiphase model simulates flows of several fluids through convective transport. This convective transport is capable of resolving the interface between all mixture phases of interest if the high-resolution interface capturing (HRIC) scheme is enabled. The k-Epsilon model is a two-equation turbulence model that solves for the turbulent kinetic energy and turbulent dissipation rate to determine the turbulent eddy viscosity. The segregated multiphase temperature model simulates the thermal effects in the simulation through solving the total energy equation for temperature. Finally, the average mushy-zone permeability model is a volume-weighted model of the mixture inside the lithium bath. This model allows for control over a phase's change of state by modeling the solidifying phase as decreasing in porosity as the solid volume fraction of a phase increases. The melting-solidification sub-model was enabled so that the molten phase could solidify once cooled to its freezing temperature. A surface tension was enabled for the Li-CO_2, Li_2C_2-CO_2, and Li_2O-CO_2 interactions inside the model. Each of these interactions had a surface tension of 0.3 N/m with the goal of creating, to a small degree, the beginning parts of surface tension modeling.

The VOF model remained as its default first-order convection for all models that were analyzed. The HRIC property was not selected even though it provided higher resolution to the product species because the model would occasionally suffer from lithium conservation issues. Gravity was included in the model in the direction consistent with the orientation of the experimental reactor.

3.3. Material Properties

In the multiphase material model, six species, CO_2, Li, Li_2C_2, Li_2O, Li_2CO_3, and C were treated as separate phases. The molecular weight, specific heat, and density of each species was specified. The values for each species can be found in Table 1.

Table 1: Properties of species inside the reactor

Species	Molecular Weight (kg/kmol)	Density (kg/m^3)	Specific heat (J/kg-K)
CO_2	44.0087	-	850.57
Li	6.941	534	4155.02
Li_2C_2	37.9034	1300	2275.52
Li_2O	29.881	2010	2886.45
Li_2CO_3	73.8897	2110	2509.62
C	12.0107	950	675.231

For the condensed phases, constant properties were assumed, and each phase was assumed to be immiscible. The CO_2 density is not listed in this table because it was modeled using the ideal gas law. The lithium species was treated as a molten material and was assumed to have a constant density. Likewise, the product species, Li_2C_2, Li_2O, Li_2CO_3, and C, were all defined similarly to the lithium species, except melting-

solidification and mushy-zone permeability were selected as additional optional models. The solidus and liquidus temperatures of each species undergoing melting-solidification were defined. Below the solidus temperature, the species will be modeled as a solid and above the liquidus temperature the species will be modeled as a liquid. If the species is at a temperature between the solidus and liquidus temperature, both melting and solidification occur in the species. As a product species begins to solidify, the mushy-zone permeability model turns on which increases the flow resistance in the applicable cells. With a higher flow resistance, the solidifying fluid becomes less permeable as it freezes until the species has reached its lowest permeability value upon reaching the solidus temperature.

3.4. Model Geometry

The domain of the model was sketched in 2D on the X-Y plane, where X was designated as the axial direction and Y the radial direction, using the native sketching feature in Star-CCM+. In total, three sketches were created that define the CO_2 Injection Tube, Reactor, and Wall regions (Figure 2). Once each specific region was sketched, gridded, and had its physics fully defined, they acted as one cohesive model through conjugate heat transfer and flow boundary interfaces.

Each sketch in this model corresponds to an individual region. A region in Star-CCM+ is a discrete domain in the model that contains individual boundary conditions, phase conditions, and physics conditions that define how the model operates locally. The model was broken into three distinct regions for ease of operation when determining the

boundary conditions and initial conditions associated with each part of the reactor. Together, the CO_2 Tube and the Reactor regions form the molten combustor interior, and the Wall region forms the solid combustor shell. The CO_2 Tube and Reactor regions therefore use the multiphase material physics, and the Wall region therefore uses the solid material physics.

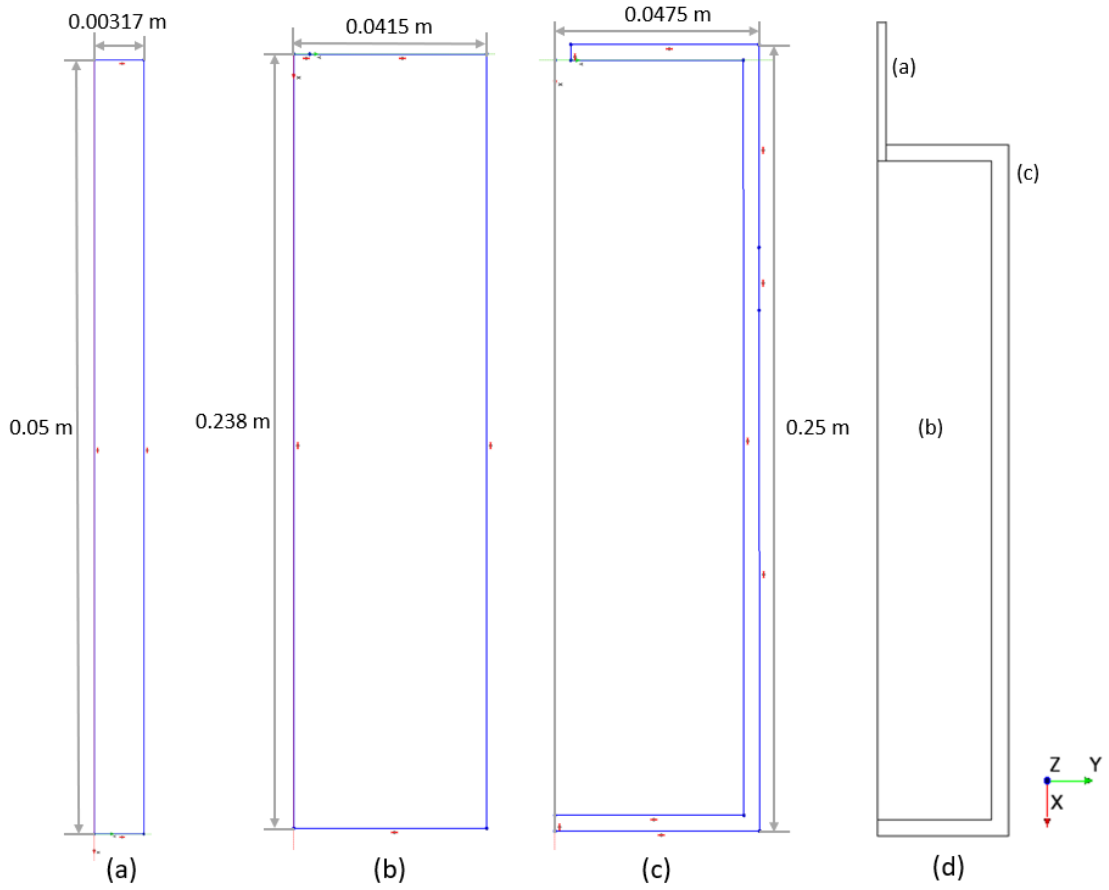

Figure 2: Sketches (a), (b), and (c) are the three sketches in the model that create the CO_2 Injection Tube, Reactor, and Wall regions, respectively, (d) is an assembly of all the sketches put together

The direction of gravity is positive in the positive X direction. The 2D axisymmetric model was used because it was a reasonable approximation of the combustor. The CO_2 injection tube in the experiment was placed along the centerline of the reactor, so the axisymmetric model assumption was a reasonable assumption to make.

The dimensions of all three sketches were modeled after the dimensions of Reactor 3.0 and Reactor 3.2 which Greer et al. [5] have outlined in their paper. A rendering of Reactor 3.0 is shown in Figure 3.

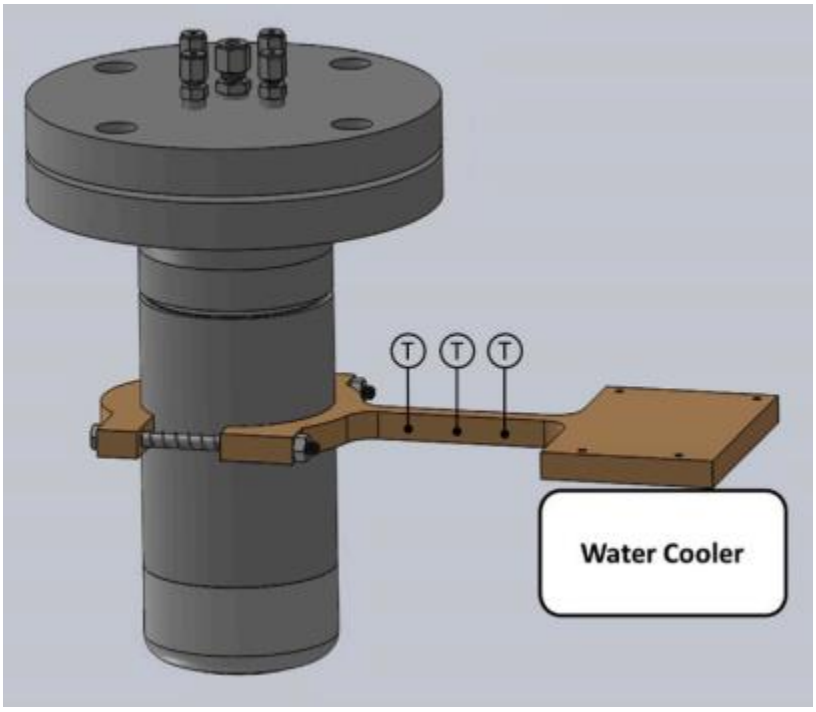

Figure 3: Rendering of modeled reactor. Clamp attachment for reactor cooling [5]

The CFD model reactor was sketched with a height of 0.238 m, and a radius of 0.0415 m. The radius of the oxidizer injector tube was 0.00317 m, with an arbitrarily chosen length that was long enough to ensure the oxidizer flow was fully developed

before entering the reactor. The wall of the reactor has a thickness of 0.006 m. These measurements matched the experimental combustor geometry.

Figure 4 shows the model with all three sketches that were used to conduct these simulations combined into one cohesive unit.

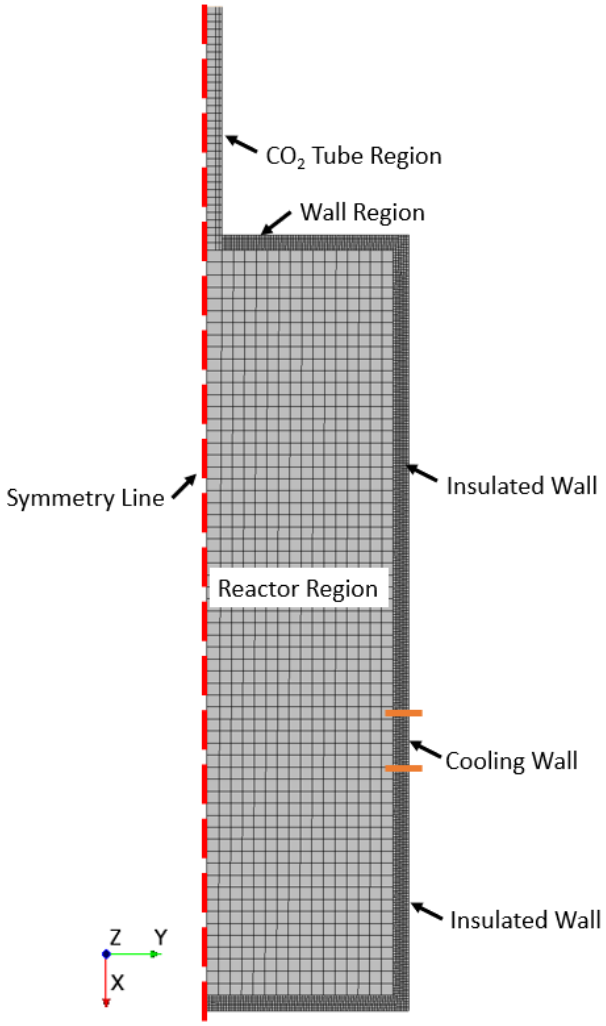

Figure 4: Domain of the model showing the CO_2 Tube, Reactor, and Wall regions, with some wall boundaries identified

Inside the CO_2 Tube region, the only species present upon initialization is CO_2. Inside the Reactor region, only CO_2 and lithium exist upon initialization of the

simulation. After the simulation has begun, the product species Li_2C_2, Li_2O, Li_2CO_3, and C start to form inside the Reactor region. At the start of the simulation, the reactor contains approximately 67% CO_2 headspace and 33% lithium by volume. The Reactor region receives CO_2 from the CO_2 Tube at 300 K that then combusts with the lithium bath.

The Wall region seen in Figure 4 is modeled with the properties of 316 stainless steel, reflecting the composition of the reactor walls of the experimental tests. This region is further split into simulated insulation sections and a simulated cooling section using boundary conditions.

3.5. Boundary conditions and initial conditions

The initial conditions for the combustion region were an initial pressure of 15000 Pa absolute, a static temperature of 1173 K, a velocity of 0 m/s in the axial and radial directions and an initial height of molten lithium of 0.07 m, which corresponds to approximately 200 g of lithium. Further, only CO_2 and lithium species are present upon initialization. The initial condition for the combustor wall was a static temperature of 1173 K to match the initial static temperature of the lithium bath. These values were chosen because they reflected startup conditions of the reactor during the experimental test which was modeled in CFD.

The boundary conditions are specific to each region. The four types of boundary conditions in the CO_2 Tube region are pressure outlet, axis, wall, and interface boundary

conditions. Figure 5 shows the location of each boundary condition of the CO_2 Tube region.

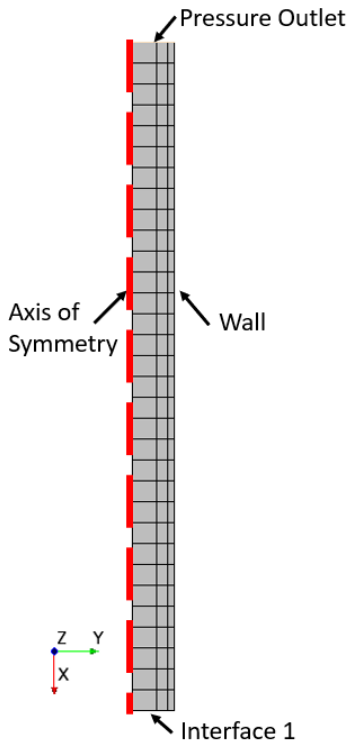

Figure 5: Boundary conditions of the CO_2 Tube region that shows the location of the mass flow inlet (pressure outlet), axis of symmetry, wall, and interface with the Reactor region

The pressure outlet boundary condition was chosen instead of the mass flow inlet boundary condition because the pressure outlet boundary condition provided the option to choose a target mass flow rate and a target pressure. The target mass flow rate and target pressure options allowed for a more realistic representation of the mass flow rate and pressure inside the reactor as observed in the experimental tests. With this boundary condition, the mass flow into the combustor would be able to increase or decrease in

response to the current rate of CO_2 consumption in the reactor. The mass flow entering the reactor could therefore change to react to the changing conditions inside the reactor.

The Pressure outlet boundary condition is an outflow condition which can apply a correction to the pressure boundary value so that a specific mass flow rate could be achieved. Even though this boundary condition is an outflow condition, it can be used in cases of reverse flow (i.e. inlet). The CFD model takes advantage of the reverse flow condition to create CO_2 inflow into the system which is capable of targeting both a mass flow rate and a target pressure.

The pressure outlet boundary condition was chosen to have a target mass flow rate of 2.37E-5 kg/s. This definition of mass flow best matched the average mass flow of the Greer et al. Reactor 3.2 experiment [5]. Reactor 3.2 varied in mass flow throughout the duration of the reaction, frequently rising significantly above and falling significantly below the average target mass flow. This mass flow variation was achieved through the manual use of a mass flow controller. The CO_2 flow was throttled as necessary to lower or raise the rates of reaction inside the reactor so that the reactor temperature would remain at acceptable levels.

The wall boundary condition of the CO_2 Injection Tube contains a no slip condition. This wall separates the oxidizer in the CO_2 Tube from the ambient atmosphere. An interface boundary condition between the CO_2 Tube region and the Reactor region is also used. The internal interface boundary condition in Figure 5 interfaces with an internal interface boundary condition of the same size in the Reactor region which allows the oxidizer in the CO_2 Tube to enter the headspace in the Reactor region. This interface was included in the model to assist in the purposes of meshing each region separately

because a single mesh could not be generated for the entire model that satisfied necessary requirements in both the CO_2 Tube and Reactor regions.

This separate meshing was useful when the Courant number was used to define the time stepping of the model. The Courant number was only defined in the Reactor region of the model. Creating two regions allowed for the CO_2 Tube to have a coarser mesh than the reactor region. The goal of the CO_2 Tube was only to create fully developed flow into the reactor without limiting the time stepping of the model. Therefore, the model could have a coarser mesh in the CO_2 Tube region to increase time stepping because it would not impact the development of fully developed flow. Therefore, two separate mesh regions were required, and an interface was necessary so that information could pass between the meshes.

Usually, if there is an inlet to the system in a model there will also be an outlet. In this model there is no outlet because no outlet is necessary. The experimental test took advantage of the chemistry of the reaction which ensures that there is no gas combustion product, and the products are denser than the reactants. Because of this, the products usually sink to the bottom of the reactor without any gas build-up resulting from combustion. This resulted in the unusual situation where no outlet boundary condition was required for successful operation of the model.

The Reactor region has wall, axis of symmetry, and interface boundaries. Being in contact with both the CO_2 Tube and Wall regions, all the wall boundary conditions in the Reactor region are internal interfaces to facilitate the passage of information between regions. Figure 6 depicts the location and type of each boundary condition for the Reactor region.

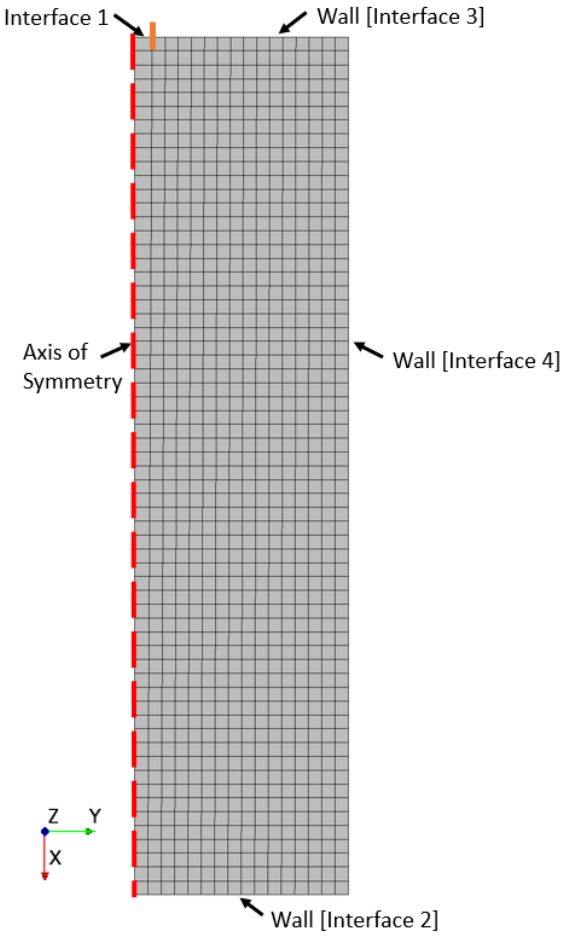

Figure 6: Boundary conditions of the Reactor region showing the location of the interface connections to the other regions and the axis of symmetry boundary condition

The Reactor region is surrounded on three sides by the Wall region at interfaces 2 through 4 as described by Figures 6 and 7 and contacts the CO_2 Tube region at interface 1 as described by Figure 5 and 6. The length of interface 1 is one cell wide as emphasized by the thick line separating interface 1 and interface 3 in Figure 6. Because the Reactor region is in contact with both the CO_2 Tube and Wall region, every boundary in the Reactor region contains an interface that interacts with another specified region. Specifying an interface between regions was necessary so that information from one

region can pass into the other regions. As with the CO_2 Tube region, the axis boundary condition is an axis of symmetry. This axis boundary condition of the Reactor region in Figure 6 aligns with the axis boundary condition of the CO_2 Tube in Figure 5.

Finally, the Wall region was created to model the wall of the experimental reactor and functioned as a heat sink for the heat generated in the Reactor region and facilitated heat transfer in the model. The thickness of the wall was made the same as the wall thickness of the experimental combustor. This Wall region allowed for heat to dissipate through the wall and also acted to redistribute the heat inside the combustor. The Wall region contains the wall and axis boundary conditions. Figure 7 depicts the locations of these boundary conditions for the Wall region with a dotted line for the axis of symmetry.

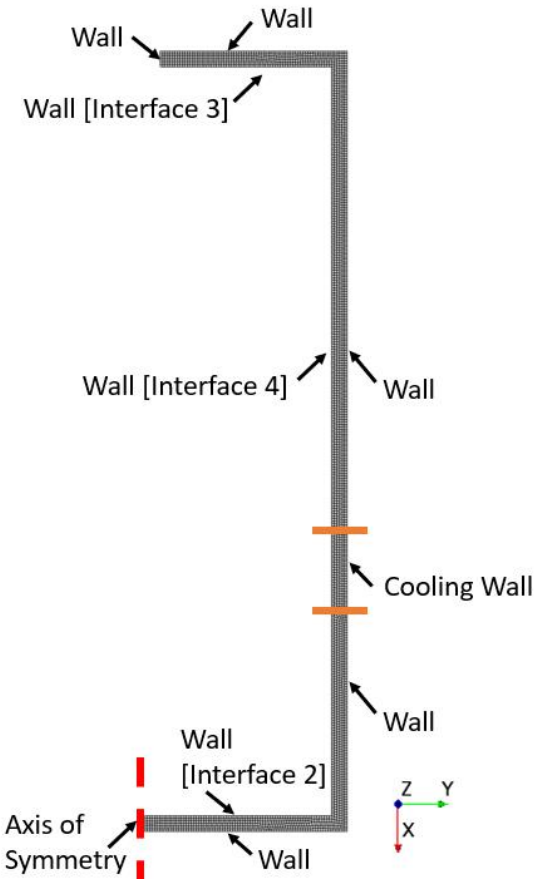

Figure 7: Boundary conditions of the Wall region showing the location of the wall interface sections to the Reactor region and the axis of symmetry boundary condition

By means of conjugate heat transfer, the inner walls interface with the Reactor region and pass thermal information between the Wall region and Reactor region. Every outer wall is insulated as in the experiments to prevent heat loss, except for a small section of the wall that simulates the cooling clamp as can be seen in Figure 3 and Figure 4. All outer walls use a convective boundary condition.

Because the convective boundary condition is used across the entire wall of the combustor, a convection coefficient of 1 W/m^2-K was chosen to represent highly

insulated walls and 91.09 W/m^2-K was chosen to represent the cooling clamp section of the wall because these values approximated the values from Greer et al. [5]. Additionally, the ambient temperature surrounding the reactor was 300 K which best matched the ambient conditions of the experimental reactors. The cooling clamp convection coefficient value was chosen to provide an accurate representation of the cooling conditions recorded in Reactor 3.0 and Reactor 3.2 from the experiments conducted by Greer et al. [5]. The cooling clamp was a copper clamp used in the experimental tests which was placed at the initial free surface of the molten lithium bath. The clamp simulated heat being acquired for use in a Stirling engine and also helped prevent the combustor from overheating.

3.6. Field function calculations

Within the model, field functions were created to define source terms in Equations (4) to (6). Some of these terms define the reaction rate of each reaction, others define the heat generated from the three reactions, and others calculate the overall mass of each element in the reactor as a conservation of mass check to ensure conservative properties are properly being abided. Source terms for calculating the overall degree of completion of each reaction were also developed for the tracking of each reaction, and therefore also the overall heat generation.

Each reaction needed an equation that dictated the rate at which each reaction would commence. The rates of each reaction are defined as

$$\text{Reaction 1}: \quad \chi_{Li} * \chi_{CO_2} * 200 * \rho_{CO_2} \tag{7}$$

$$\text{Reaction 2}: \quad \chi_{Li_2C_2} * \chi_{CO_2} * 40 * \rho_{CO_2} \tag{8}$$

$$\text{Reaction 3 Positive}: \quad (-0.02 * T + 21.46) * \chi_{Li_2O} * \chi_{CO_2} * 20 * \rho_{CO_2} \tag{9}$$

$$\text{Reaction 3 Negative}: \quad (0.02 * T - 20.46) * \chi_{Li_2CO_3} * 0.5 * \rho_{Li_2CO_3} \tag{10}$$

where χ is the volume fraction of the species, ρ is the density of the species and T is the temperature of each cell in the reactor. Equation (7) is the rate of lithium destruction (Reaction 1) between lithium and CO_2 which forms Li_2C_2 and Li_2O. Equation (8) is the rate of lithium carbide destruction (Reaction 2) between Li_2C_2 and CO_2 which forms Li_2CO_3 and C. Equation (9) is the rate of lithium oxide destruction (Reaction 3 positive) between Li_2O and CO_2 in the forward direction, and equation (10) is the rate of lithium oxide and CO_2 formation (Reaction 3 negative), through the dissociation of Li_2CO_3. Equation (9) takes Li_2O and CO_2 to produce Li_2CO_3 and equation (10) takes Li_2CO_3 and disassociates it back into Li_2O and CO_2 at temperatures above 800°C [27].

These reactions occur only in the cells which contain both a presence of the applicable fuel and CO_2. Therefore, the reactions will commence more vigorously in cells located at the surface of the lithium bath because there is a higher presence of both fuel and CO_2 volume fraction in those cells. Away from the lithium bath surface, in the headspace or deep in the lithium bath, a reaction can still commence, but either the presence of fuel or CO_2 will be lacking in those cells which will limit the rate at which the reaction can commence in those cells. Therefore, it is assumed that a reaction can occur anywhere inside the combustor so long as there is a presence of both a fuel and CO_2.

The coefficients before the density term in equations (7)-(10) represent parametric fits to the model reaction rates that best produced a similar amount of product yield that was observed in experimental tests. Each of the coefficients were adjusted manually and the proper values were determined over multiple iterations of the model's development until a yield best comparable to Reactor 3.2 was achieved. These rates of reaction were defined specifically for the combustion of the metal fuel specific to each reaction. Other species production or destruction is governed through stoichiometry. The rate for each reaction is defined for every cell in the reactor region. For any reaction to commence in any cell of the model, both reactants must be present in the cell. An additional requirement was included in equations (9) and (10), where the temperature in the cell must be at an appropriate level before either reaction could commence.

The forward reaction of Reaction 3 is most active at temperatures below 750°C and shuts off at 800°C, decreasing at a linear rate between these two temperatures. The negative reaction of Reaction 3 does the opposite. Reaction 3 negative is off at temperatures below 750°C and is fully on at temperatures above 800°C, increasing linearly between these two temperatures. This temperature range was chosen so that there was a smoother transition between Li_2CO_3 production and Li_2CO_3 disassociation for modeling purposes. So, at temperatures below 750°C Li_2CO_3 is being produced and at temperatures above 800°C Li_2CO_3 is being disassociated, with a mix of both reactions occurring at the intermediate temperatures.

The units of equations (7)-(10) are kg/m^3-s. These rates, along with the mass flow of CO_2, dictate how fast these reactions will progress inside the reactor and therefore how much heat will be generated at any given moment of the reaction.

Because all three reactions generate heat at varying amounts, the heat of reaction for each reaction was computed. However, because Star-CCM+ calculates enthalpy *differences* instead of total enthalpy, the de facto reference temperature becomes 0 K instead of 298.15 K. Therefore, careful consideration was required to ensure the heat of reaction calculation was carried out for a 0 K reference temperature. As a result, the equations for the heat of reaction (ΔH_{rxn}) in J/kg_{fuel} for Reactions 1 through 3, and the decomposition of Li_2CO_3 are calculated as

$$\Delta H_{rxn,1} = \frac{2}{5}\frac{MW_{Li_2O}}{MW_{Li}}\left(h_{f,Li_2O,(298)} + 298 * C_{p,Li_2O}\right) + \frac{0.5}{5}\frac{MW_{Li_2C_2}}{MW_{Li}}\left(h_{f,Li_2C_2,(298)} + 298 * C_{p,Li_2C_2}\right) - 1\left(h_{f,Li,(298)} + 298 * C_{p,Li}\right) - \frac{1}{5}\frac{MW_{CO_2}}{MW_{Li}}\left(h_{f,CO_2,(298)} + 298 * C_{p,CO_2}\right) \quad (11)$$

$$\Delta H_{rxn,2} = \frac{MW_{Li_2CO_3}}{MW_{Li_2C_2}}\left(h_{f,Li_2CO_3,(298)} + 298 * C_{p,Li_2CO_3}\right) + \frac{5}{2}\frac{MW_{C}}{MW_{Li_2C_2}}\left(h_{f,C,(298)} + 298 * C_{p,C}\right) - \frac{3}{2}\frac{MW_{CO_2}}{MW_{Li_2C_2}}\left(h_{f,CO_2,(298)} + 298 * C_{p,CO_2}\right) - 1\left(h_{f,Li_2C_2,(298)} + 298 * C_{p,Li_2C_2}\right) \quad (12)$$

$$\Delta H_{rxn,3\ pos} = \frac{MW_{Li_2CO_3}}{MW_{Li_2O}}\left(h_{f,Li_2CO_3,(298)} + 298 * C_{p,Li_2CO_3}\right) - \frac{MW_{CO_2}}{MW_{Li_2O}}\left(h_{f,CO_2,(298)} + 298 * C_{p,CO_2}\right) - 1\left(h_{f,Li_2O,(298)} + 298 * C_{p,Li_2O}\right) \quad (13)$$

$$\Delta H_{rxn,3\ neg} = \frac{MW_{Li_2O}}{MW_{Li_2CO_3}}\left(h_{f,Li_2O,(298)} + 298 * C_{p,Li_2O}\right) + \frac{MW_{CO_2}}{MW_{Li_2CO_3}}\left(h_{f,CO_2,(298)} + 298 * C_{p,CO_2}\right) - 1\left(h_{f,Li_2CO_3,(298)} + 298 * C_{p,Li_2CO_3}\right) \quad (14)$$

where C_p and h_f are the specific heats and enthalpies of formation at 298 K for each species of interest, and MW is the molecular weight of the species of interest. The enthalpies of formation and specific heats were obtained from the National Institute of Standards and Technology (NIST) Chemistry website [28], which can be seen in Table 2.

Table 2: Specific heats and enthalpies of formation for selected species

Species	Specific Heat (J/kg-K)	Enthalpy of Formation, h_f (J/kg)
Li	4155.02	0
CO_2	1233.92	-8.942E6
Li_2O	2886.45	-18.515E6
Li_2C_2	2275.52	-14.596E6
Li_2CO_3	2509.62	-15.903E6
C	675.23	0

Additionally, the heat of reaction for all three reactions, plus the decomposition reaction has been collated into Table 3. The reported heat of reaction values are calculated from equations (11)-(14).

Table 3: Heat of reaction for each reaction

Reaction Number	Heat of Reaction (J/kg_{fuel})
Reaction 1	-28.37E6
Reaction 2	-13.74E6
Reaction 3 Positive	-7.19E6
Reaction 3 Negative	2.91E6

The rate of change (RoC) of each species, units of 1/sec, was then calculated as a source term for the volume of fluid equations to determine how much of a species was either created or destroyed in the combustion process. The rate of change calculation was computed as

$$RoC_i = R_{1,2,or\ 3} * \frac{\frac{MW_i * N_i}{MW_{fuel} * N_{fuel}}}{\rho_i} \quad (15)$$

where i denotes the species of interest, MW_{fuel} is the molecular weight of the fuel for the particular reaction, ρ_i is the density of the species of interest, N_i is the number of kilomoles of species i, and $R_{1,\ 2,\ or\ 3}$ is the reaction rate of the first, second, or third reaction as described in the beginning of this section.

The stoichiometry for each rate of change equation was accounted for through the ratio of kilomoles of the species of interest to the kilomoles of fuel. Each molecular weight was multiplied by a scalar corresponding to how many kilomoles of substance

there is in a particular reaction as defined in equations (1)-(3). The division by density was included to convert this equation from a mass calculation to a volumetric calculation. This conversion was necessary because of how Star-CCM+ defines species source terms within the VOF model. This rate of change calculation was done for every species in every reaction, both reactants and products, totaling 11 different equations across all three reactions. A further three equations were created to describe the decomposition of Li_2CO_3 at elevated temperatures.

The energy values from each of these reactions were then multiplied by the density of the fuel of that particular reaction so that the heat of reaction could be calculated on a volume basis instead of a mass basis, as required by Star-CCM+. The equation for converting from a mass basis (ΔH_{rxn}) in equations (11)-(14) to a volume basis (Q_{rxn}) is

$$Q_{rxn} = \Delta H_{rxn} * \rho_{fuel} \tag{16}$$

where Q_{rxn} is the heat of reaction on a volume basis in J/m^3. This conversion was completed because it was required for implementation into Star-CCM+.

Because one model validation check involves tracking the thermal yield of the simulation, it was important to track the degree of completion of all three reactions. The degree of completion for each reaction will help predict how much progress each reaction has made in consuming fuel and producing products, which determines the overall thermal yield. The completion rates of the experimental tests have been estimated by Greer et al. [5], so tracking the completion rate of the model is an important comparison with test results. The degree of completion for each reaction ($f_i(t)$) was computed as

$$f_1(t) = \frac{\int_{t=0}^{t}\left(\oint_V R_1 dV\right)dt}{M_{Li}} \tag{17}$$

$$f_2(t) = \frac{\int_{t=0}^{t}\left(\oint_V R_2 dV\right)dt}{CM_{Li_2C_2}} \tag{18}$$

$$f_3(t) = \frac{\int_{t=0}^{t}\left(\oint_V R_3 dV\right)dt}{CM_{Li_2O}} \tag{19}$$

where M_{Li} is the mass of lithium, CM_i denotes the created mass of either Li_2C_2 or Li_2O based off the progression of the first reaction, and R_1, R_2, and R_3 are the reaction rates of each reaction. CM_i was calculated, for Reaction 1, for instance, as

$$CM_{Li_2C_2} = f_1 * \frac{M_{Li,i}}{MW_{Li}} * \frac{0.5}{5} * MW_{Li_2C_2} \tag{20}$$

$$CM_{Li_2O} = f_1 * \frac{M_{Li,i}}{MW_{Li}} * \frac{2}{5} * MW_{Li_2O} \tag{21}$$

where $M_{Li,i}$ is the initial mass of lithium in the system upon initialization and f_1 is the degree of completion of Reaction 1.

The heat generated from the model also needed to be tracked. Once again, using Reaction 1 as an example, the maximum total heat that could be produced from the reaction ($Q_{max,1}$) was calculated by multiplying the heat of reaction by the total mass of lithium that was initialized in the system, which provided the equation

$$Q_{max,1} = Q_1 * M_{Li,i} \tag{22}$$

where Q_1 is the heat of reaction of Reaction 1 and $M_{Li,i}$ is the initial mass of lithium. Obtaining the total possible heat generated for the second and third reactions is slightly different from the calculation for the first reaction because the second and third reactions

are dependent upon the rate of product formation from the first reaction and are therefore dependent upon the degree of completion of the first reaction. Therefore $Q_{max,2}$ and $Q_{max,3}$ are defined as

$$Q_{max,2} = \left(f_1 * \frac{M_{Li,i}}{MW_{Li}} * \frac{0.5}{5} * MW_{Li_2C_2}\right) * Q_2 \tag{23}$$

$$Q_{max,3} = \left(f_1 * \frac{M_{Li,i}}{MW_{Li}} * \frac{2}{5} * MW_{Li_2O}\right) * Q_3 \tag{24}$$

where MW denotes the molecular weight of the species, f_1 denotes the degree of completion of Reaction 1, and Q denotes the heat of reaction for each reaction.

Equations (22)-(24) were then used to obtain the overall thermal yield (Q_{yield}) that is theoretically possible from the model. The overall thermal yield equation is calculated as

$$Q_{yield} = \frac{f_1 * Q_{max,1} + f_2 * Q_{max,2} + f_3 * Q_{max,3}}{Q_{max,1} + Q_{max,2} + Q_{max,3}} \tag{25}$$

From this equation, the total thermal yield of the system is obtainable. The value obtained from the thermal yield equation can then be compared to the experimental results and can be further used for evaluating the accuracy of the model.

Additionally, to ensure the model was accurately conserving the elements of interest, the total mass of lithium, carbon, and oxygen (M_{Li}, M_C, and M_O) were calculated. The total mass of Li, C and O were calculated as

$$M_{Li} = V\rho\ (Y_{Li} * \frac{MW_{Li}}{MW_{Li}} + Y_{Li_2C_2} * 2\frac{MW_{Li}}{MW_{Li_2C_2}} + \ Y_{Li_2O} * 2\frac{MW_{Li}}{MW_{Li_2O}} + Y_{Li_2CO_3} * 2\frac{MW_{Li}}{MW_{Li_2CO_3}}) \quad (26)$$

$$M_C = V\rho(Y_{CO_2} * \frac{MW_C}{MW_{CO2}} + Y_{Li_2C_2} * 2\frac{MW_C}{MW_{Li_2C_2}} + \ Y_C * \frac{MW_C}{MW_C} + Y_{Li_2CO_3} * \frac{MW_C}{MW_{Li_2CO_3}}) \quad (27)$$

$$M_O = V\rho(Y_{CO_2} * 2\frac{MW_O}{MW_{CO2}} + Y_{Li_2O} * \frac{MW_O}{MW_{Li_2O}} + Y_{Li_2CO_3} * 3\frac{MW_O}{MW_{Li_2CO_3}}) \quad (28)$$

where V and ρ, are the volume and density of each cell, and Y is the mass fraction of every species that contains the element of interest. The M_{Li} value is being compared against the initial mass of lithium in the system. If the system is properly conserved, this number should not change. The M_C and M_O values are being compared against the mass flow rate of CO_2 entering the system. Likewise, if these values are to be properly conserved M_C and M_O should increase at a rate equivalent to the rate of all C and O introduced into the system from the CO_2 oxidizer. This calculation was necessary to make sure that atoms of C, O, and Li were being conserved within the system and were not being created or destroyed through inaccurate stoichiometry, numerical errors introduced from a time step that was too large, too few inner iterations, or from too coarse of a mesh.

Additionally, a slip velocity term was important to incorporate because this term eliminated non-physical results which would occur when the lithium level dropped from

one grid row to the next in the model. Every time the molten lithium was reduced by one row of cells, Reaction 1 would spike and slowly reduce in rate before the same action occurred when the lithium dropped to the next row of cells. This phenomenon occurred because as CO_2 became more present in the cell as the lithium was used up, the reaction rate would fall. Once all the lithium was used up in a cell, the reaction moved to the next cell below where there was a low presence of CO_2. This low presence of CO_2 in the cell caused the reaction rate to spike until CO_2 could make its way into the cell. To fix this issue, the slip velocity equation was created which allowed CO_2 to penetrate slightly into the lithium bath. This drift velocity term represents a slightly diffuse reaction front by allowing the CO_2 to penetrate into the free surface of the lithium bath. This slightly diffuse reaction front provided a minor presence of CO_2 in each applicable cell, which was enough to heavily reduce the unphysical spikes in the reaction rates.

The drift velocity equation that was incorporated into the model was:

$$1E-6 * \frac{-\nabla \chi_{CO_2}}{\Delta t} \tag{29}$$

This equation incorporates the gradient of the volume fraction of CO_2 and divides that by the time step to calculate the slip velocity near the free surface. The slip velocity term was applied to the Li-CO_2, Li_2C_2-CO_2, and Li_2O-CO_2 phase interactions.

3.7. Domain meshing

Throughout the modeling process, the choice of meshing was an ongoing concern. Careful consideration was needed for deciding upon a mesh because of its importance in

the development of proper mass conservation. As a result, many mesh iterations were trialed.

At the beginning stages of model creation, a polygonal mesh was used, but it became apparent that this type of mesh did not provide a realistic depiction of the reaction surface and did not provide appropriate mass conservation. Therefore, a new type of mesh would need to be used to obtain better resolution in this zone. Thereon, a quadrilateral mesh was used for the greater flexibility it provided in meshing inside the rectangular region of the reactor model. Additionally, each region was meshed separately in order to maximize control over cell size and mesh resolution.

The separation of the model into three regions was important for meshing because of the unstructured meshing Star-CCM+ uses. By breaking up the model into three regions, a nearly orthogonal mesh could be more easily created in each region, which also helped in calculating the Courant number solely in the regions of interest. The calculation of the Courant number was important for understanding if information was propagating through more than one cell in a single time step, which would potentially lead to inaccurate results. It was important to calculate this number in the combustion region because the velocity of the CO_2 entering the combustion chamber needed to be monitored in the event that cell information propagated too far in a single time step once it left the CO_2 injection tube. This calculation was not important in the CO_2 injection tube itself because it was artificially long to create fully developed flow.

Further, the orthogonal mesh allowed for an easier transfer of information because irregular-shaped cells were removed from the interface of the CO_2 Tube and Reactor regions, which reduced the Courant number in the CO_2 Tube and prevented information

from skipping cells as easily as before. Additionally, the orthogonal mesh provided a better definition of the reaction zone because the layer of cells that represented the interface between the molten lithium and CO_2 upon initialization could be more easily be depicted as nearly flat. Other meshes represented the reaction zone as slightly curved towards the wall of the reactor, or slightly bulging towards the center of the reactor, which was believed to produce inaccurate results.

Additional modifications were made to the mesh which included a finer mesh in the reaction zone. The goal of the finer mesh was to increase the model fidelity in the reaction zone so that the reaction between the fuel and the CO_2 would occur across more than one cell to prevent cell information from skipping over the reaction zone entirely.

Ultimately, it was decided that this fine mesh region did not provide any benefit to the model, and so a nearly orthogonal mesh of 0.0025m by 0.0025m was chosen to be the mesh size inside the entirety of the Reactor region. The Wall region used a mesh size of 2.5E-5m by 2.5E-5m to accurately capture the temperature gradient along the reactor-wall interface and inside the wall itself. The CO_2 Tube region used a nearly orthogonal mesh of 0.004m by 0.004m, but also included a prism layer to increase the accuracy of the solution due solving for near-wall effects. The prism layer was used here to reduce the Courant number and increase the accuracy in calculating the amount of CO_2 that was entering the reactor. The Courant number was reduced in the cells affected by the prism layer because the prism layer created rectangular columns of cells that were oriented in the direction of the incoming CO_2 flow. The mesh of the entire domain is provided in Figure 8. The mesh sizes in the model were chosen as a compromise between accuracy of results and the speed at which the model could calculate results.

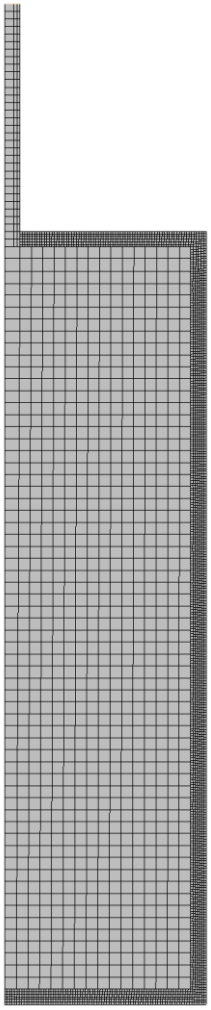

Figure 8: Mesh of the computational domain

A future goal for the modeling is to conduct a mesh sensitivity test to determine the optimal mesh size for the domain. However, the resulting increase in runtime of the model due to a decrease of cell size had to be considered for the modeling done here. As previously stated, the model required approximately 1.5 weeks of wall time to simulate 1.25 hours of physical time, so it was necessary to use a coarser mesh to achieve a realistic turnaround time in results.

Chapter 4

Results

4.1. Assessment of model efficacy

One of the products of this thesis is a comparison of modeling and experimental results. Therefore, the mass flow of CO_2, the yield of products, and the amount of unreacted lithium remaining will be compared to experimental results.

Greer's Reactor 3.0 and Reactor 3.2 were run at nominal bath temperatures of 700°C and 900°C, respectively. Both reactors were the same size and contained the same 200 g mass of lithium. Both reactors also had a copper cooling clamp attached at approximately the free surface of the molten lithium to provide necessary cooling to the reactors. In these experimental tests, the mass flow was modulated to maintain the target bath temperature. The average CO_2 mass flow rate was recorded as 4 SLM for Reactor 3.0 and 4.6 SLM for reactor 3.2. Accordingly, because the baseline case will be simulating Reactor 3.2, a mass flow of 2.37E-5 kg/s was chosen as our target mass flow in the CFD model. It was found that in Reactor 3.0, a crust of products formed over the top of the molten lithium, which prevented the reaction of lithium and CO_2 from reaching completion. This crust formation was not noticed in the hotter bath temperature of Reactor 3.2, and it was determined from a CT scan that almost no unreacted lithium remained inside the reactor.

It was decided to exercise the model under the conditions of Reactor 3.2 because of the more easily interpretable results (i.e., no crust). Reactor 3.0 had a crusting issue, the modeling of which it was possible to only partially explore in the course of this thesis, as will be described below

Greer et al. [5] found that at a fuel bath temperature of 900°C, the reaction of Li and CO_2 progressed approximately 98% to completion, with the Li_2C_2 and CO_2 and Li_2O and CO_2 progressing 0-25% and 0-9% to completion, respectively. The degree of completion of these reactions were determined through CT scans and were interrogated further using ParaView. Greer et al. noted that because combustion product composition inside the reactor varied widely, it was challenging to make a direct measurement for the final completion percentage of each reaction. The heat output noted in the Greer et al. paper [5] for Reactor 3.2 was not measured directly; however, 25.6 MJ/kg_{Li} of energy was noted as being achievable based upon stoichiometry calculations.

The Greer et al. paper [5] also contains images of CT scans that depict the unreacted lithium and products that remain inside the reactor for both Reactor 3.0 and Reactor 3.2. The CFD model is able to create contour plots that can be compared to these CT scan images.

For the simulation to run accurately, the model needed to be stabilized. The simulation started with a stabilization period that lasted roughly 450 seconds and was conducted to ensure the model was stable enough to start reacting lithium and CO_2 at a more vigorous rate. This step was conducted because if the intended rate of reaction was used upon initialization, the simulation would usually crash or a non-physical growth in the amount of lithium in the reactor would occur. During model stabilization, the time

step was linearly increased from 1E-4 seconds to 0.002 seconds for the first 200 seconds and held at 0.002 seconds until model stabilization ended around 250 seconds later. The reaction rate coefficients were set to extremely low values during this time to ensure each reaction was occurring properly and to ensure that there would be negligible product formation during this time.

After the model was sufficiently stabilized, the time stepping was doubled to 0.004 seconds and the reaction rates were gradually increased to the values indicated in equations (7)-(10) so as to ensure the model remained stable and the target mass flow was being met through the parametric fit of the reaction rates.

However, the parametric fit of Reaction 3 negative was not adjusted because the rates of Reaction 1 and Reaction 2 during the first 450 seconds remained low. This prevented large amounts of Li_2CO_3 from forming inside the reactor during stabilization, which in turn prevented large amounts of Li_2CO_3 disassociation. Additionally, the reaction rate of Reaction 3 negative was never increased after stabilization to prevent nonphysical results from occurring inside the reactor. If the disassociation reaction rate was increased too much, Li_2CO_3 would disassociate too quickly and form too much Li_2O and CO_2 inside the lithium bath which would cause conservation issues and further reaction rate issues.

Due to the gradual increase in reaction rates after the simulation stabilized, there was a large spike in the volume fraction of Reaction 1 and a drop in pressure as CO_2 within the headspace of the reactor was consumed. Figure 9 depicts this large spike in Reaction 1 with the initial drop in pressure of the reactor.

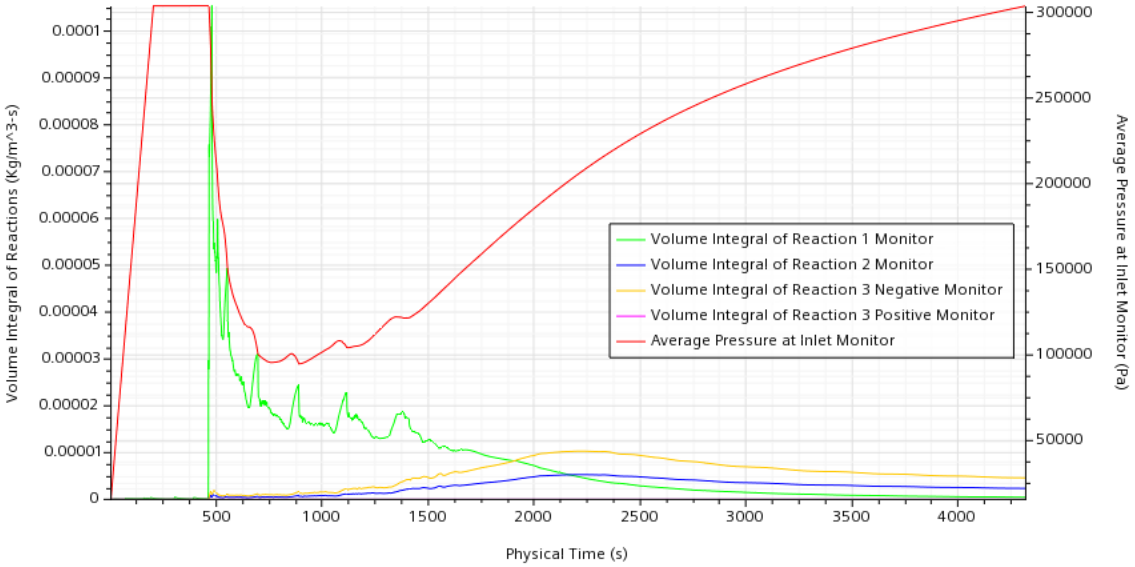

Figure 9: Plot of pressure and volume fraction of each reaction

It can also be seen in Figure 9 that the first reaction quickly dies down and eventually settles toward a steadier reaction rate with minor peaks in reaction rate occasionally occurring. Further, it can be seen in Figure 9 that Reaction 2 and the disassociation of Li_2CO_3 in Reaction 3 negative begins to increase once the first reaction creates more products and heats up the temperature of the lithium bath. As the increase in bath temperature spreads to more of the lithium bath, more lithium carbonate begins to reach the required 750-800°C temperature range to begin disassociation, as described by Equation (10), which caused the uptick of the disassociation reaction rate in Figure 9.

At the beginning of the reaction, once stabilization has finished, there is a large spike in CO_2 mass flow which is followed by smaller spikes as the mass flow begins to reach the target value. The mass flow entering the reactor and the target mass flow value can be seen in Figure 10, where the spikes of mass flow observed in Figure 10 correlate

well to the spikes of Reaction 1 observed in Figure 9. After the large spike, the mass flow rate begins to decrease towards the target mass flow rate of 2.37E-5 kg/s and settles slightly below the target with occasional spikes meeting the target value. This occurred for about 500 seconds until the first reaction begins to slow down. Once Reaction 1 began to reach completion, the mass flow rate began to decrease further below the target mass flow rate and the pressure in the combustor began to climb.

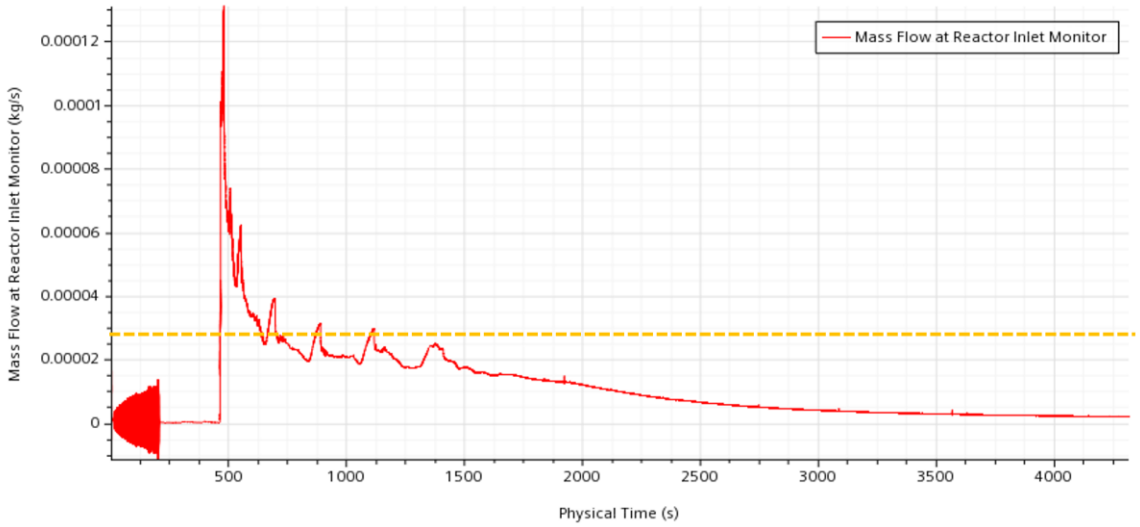

Figure 10: Plot of CO_2 mass flow entering the reactor with a dotted line depicting target mass flow

Observations were made as to the rate of product formation and the rate at which the available lithium decreases. In Figure 11, the amount of lithium carbide (Li_2C_2) has increased as expected in the beginning and middle of the simulation due to its production in Reaction 1 and decreases towards the end of the simulation due to the lithium carbide consumption of Reaction 2. It can also be seen that the majority of the product has homogeneously mixed with the lithium bath, which is a function of using the first order

Volume of Fluid (VOF) model instead of the higher-order HRIC model. The first order model was used because it resolved the mass conservation issues noted when the HRIC model was enabled. It is believed the HRIC method caused some conservation issues due to time stepping that was too large for that model to properly handle. The homogeneous mixing of lithium carbide indicates that no crust formation occurred. The same trends can be observed in the rate of lithium oxide (Li2O) formation in Figure 12.

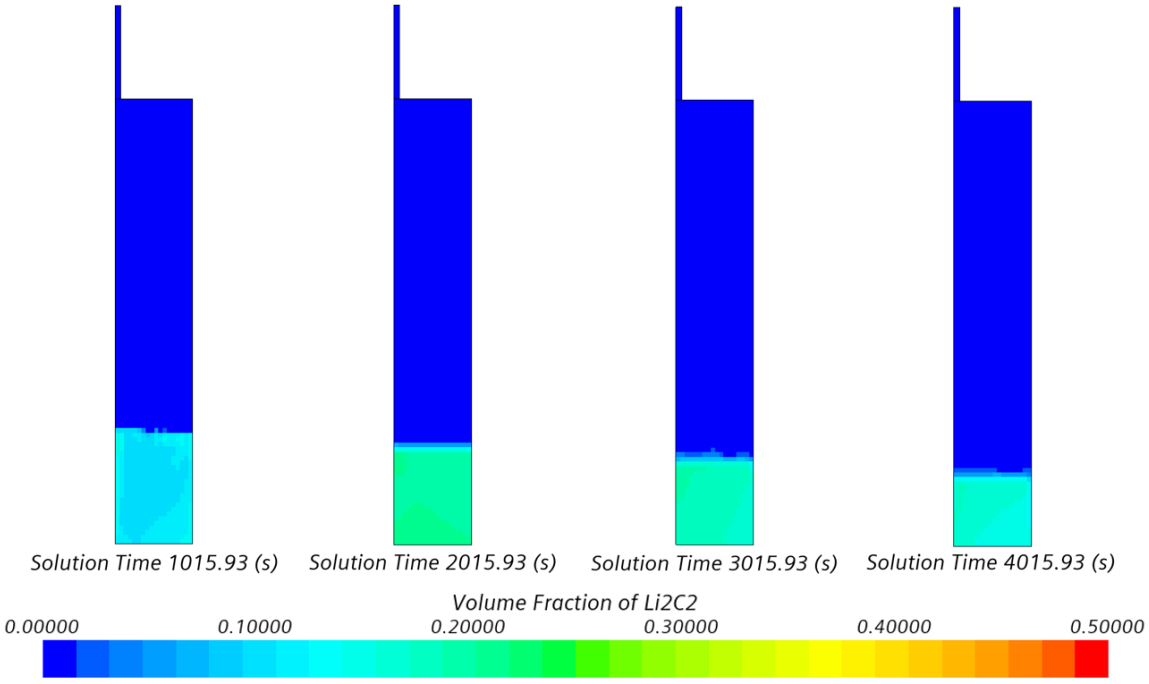

Figure 11: Volume fraction of Li_2C_2 over time

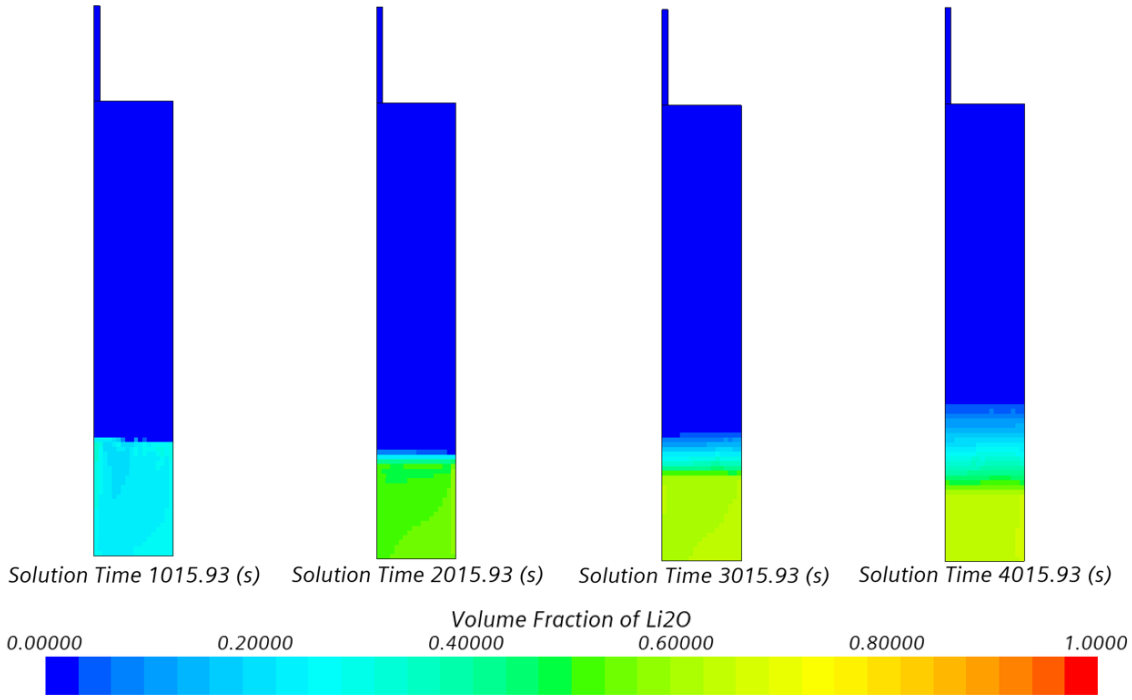

Figure 12: Volume fraction of Li_2O over time

Upon comparing Figures 11 and 12, both products have similar trends in the reported volume fractions towards the beginning of the reaction but begin to differ towards the end of the reaction. This difference is because the dissociation reaction of lithium carbonate continues to produce more Li_2O and CO_2, while Li_2C_2 is being consumed to make more lithium carbonate and carbon.

The change of the volume fraction of lithium over time is shown in Figure 13. As expected, towards the beginning of the reaction the volume fraction of lithium is large everywhere and decreases everywhere as the reaction proceeds. It is interesting to note that, for most of the middle stages of the entire reaction, a larger amount of unreacted lithium remained near the free surface as indicated in Figure 13, which is further indication that a crust formation did not occur.

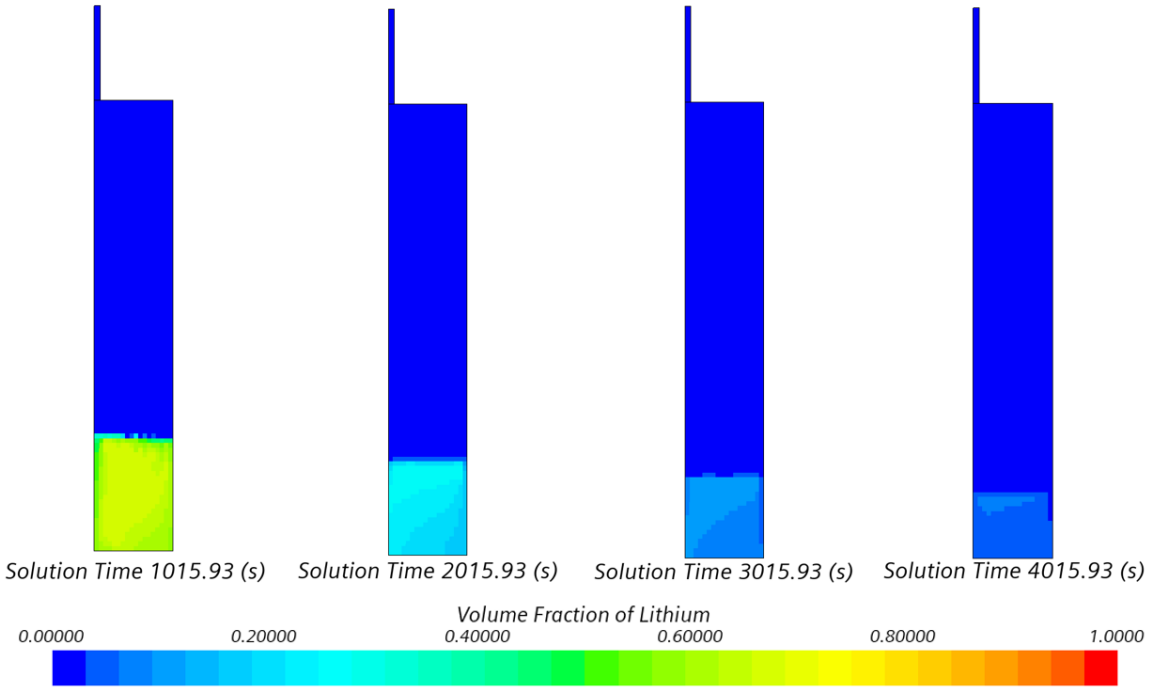

Figure 13: Volume fraction of lithium over time

Upon comparing the CFD contour plots in Figures 11 to 13 to the CT scan results of Reactor 3.2 provided in Greer et al. [5], there are a few similarities. Almost no unreacted lithium exists in either Reactor 3.2 or the model and the majority of products have deposited themselves at the bottom of the reactor. However, the CT images reveal that products have also adhered to the walls of Reactor 3.2, which is not seen in the CFD results. Inside the model, the products tended to spread out evenly due to the first-order VOF model. This is somewhat similar in behavior to what is seen in Reactor 3.2 because the majority of the products have sunk to the bottom of the reactor and mixed with each other. The CT scan of Reactor 3.2 can be seen in Figure 14 along with a comparison to the final amount of unreacted lithium and Li_2C_2 volume fraction from the model.

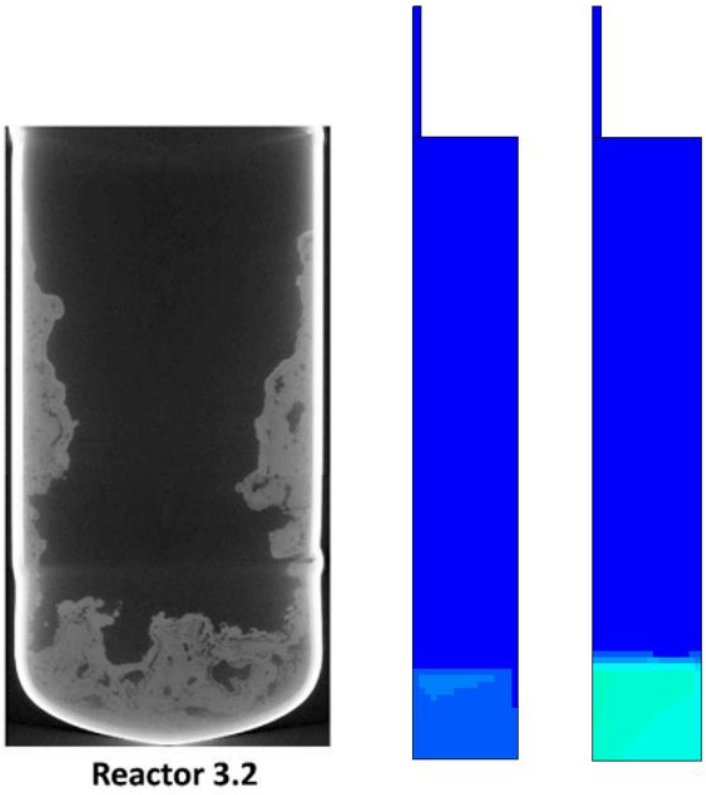

Figure 14: CT scan of Reactor 3.2 (left) from Greer et al. [5] depicting leftover products from a completed reaction alongside the unreacted lithium (middle) and Li_2C_2 product (right) from the model at the end of the simulation

The temperature results from the simulation provide insight into how the lithium bath was heated due to the reactions and provided the location of hot spots in the lithium bath. The temperature contour plots can be observed in Figure 15.

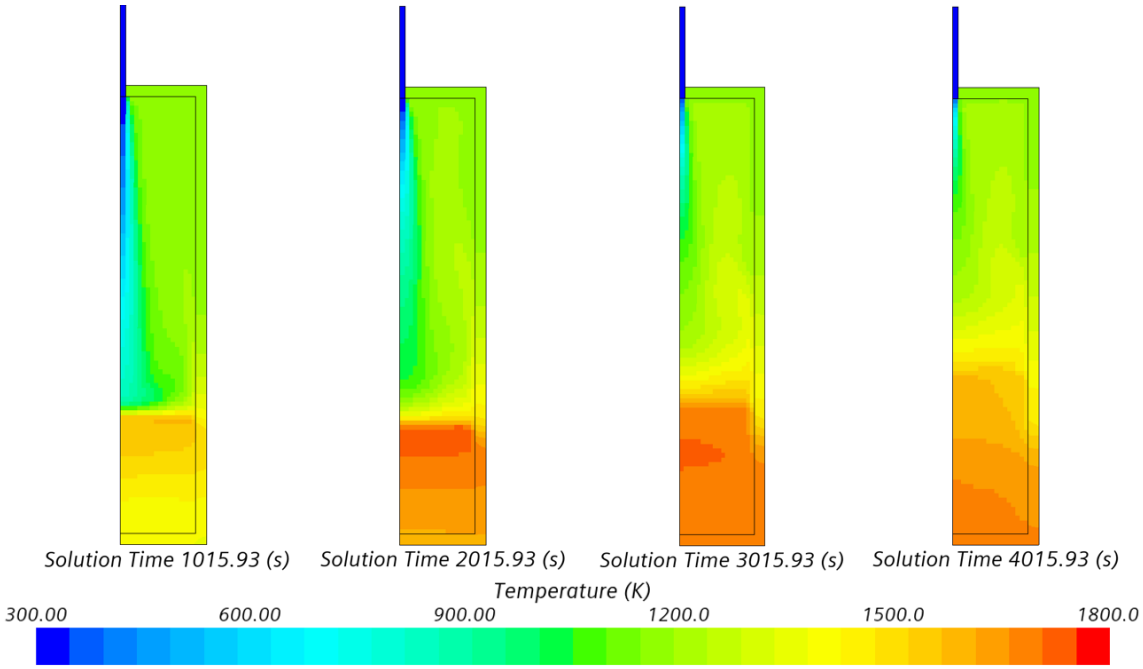

Figure 15: Temperature inside the reactor over time

The hottest portion of the reactor is located towards the free surface where each reaction is actively taking place, with slightly cooler temperatures towards the bottom of the bath. The temperature rose rapidly during the period of vigorous reaction and remained around a constant value during the remainder of the reaction. Towards the end of the reaction, the reactor began to cool down and the hottest part of the reactor transitioned to the bottom center of the reactor.

The initialization temperature in the model was equal to our targeted Reactor 3.2 experimental test to match the test's initial conditions. As there was no crust that could have slowed down the reaction chemistry, the bath temperature remained high for the duration of the simulation. It was noted that while all the reactions occurred at the free surface, once a product formed and cooled, it did not attach to the wall of the reactor to

form a crust at the surface as was observed in Reactor 3.0. Instead, the products sunk to the bottom of the lithium bath.

The total mass of Li_2C_2 and Li_2O were plotted over time to observe their trends. An indication that the reaction was nearing completion was the decline in total mass of Li_2C_2, which indicated that the first reaction was no longer producing more than what Reaction 2 was consuming. The trends of Li_2C_2 and Li_2O are plotted in Figure 16.

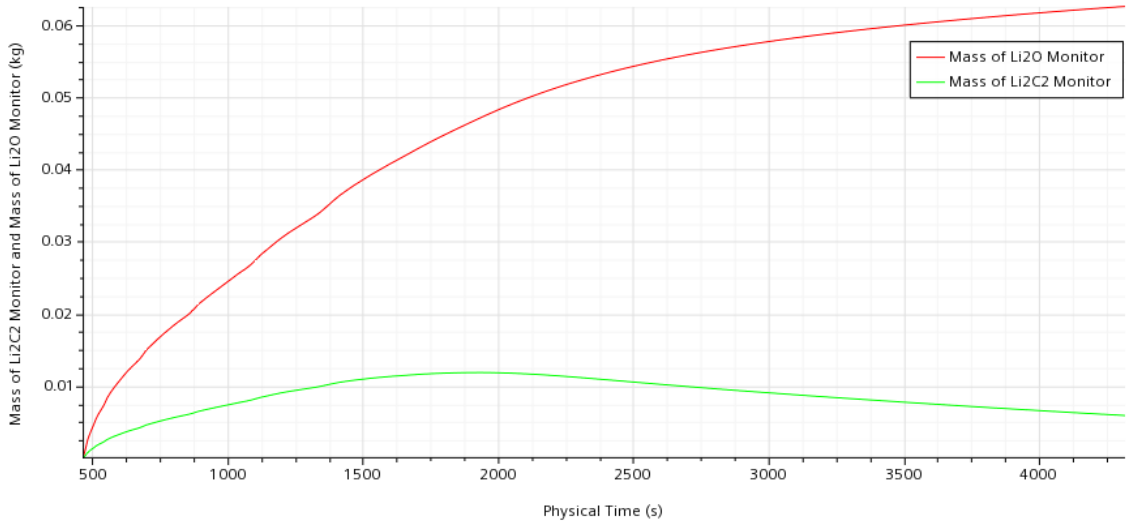

Figure 16: Plot of Li_2C_2 and Li_2O product formation inside the reactor over time

Additionally, the plot of Li_2CO_3 was used to show a depiction of how much Li_2CO_3 was still being formed and how much of it was disassociated back into Li_2O and CO_2. Figure 17 shows that Li_2CO_3 production peaked slightly after the 2000 second mark of the reaction. This peak follows slightly behind the peak mass of Li_2C_2 as recorded in the reactor in Figure 16. The Li_2CO_3 plot has a sharper decrease initially because once the bath temperature was sufficiently hot, the available Li_2CO_3 product was disassociated back into Li_2O and CO_2 at a faster rate than what Reaction 2 and Reaction 3 could

produce. The rate of Li_2CO_3 destruction begins to subside as the reaction reaches completion and the reactor begins to cool down.

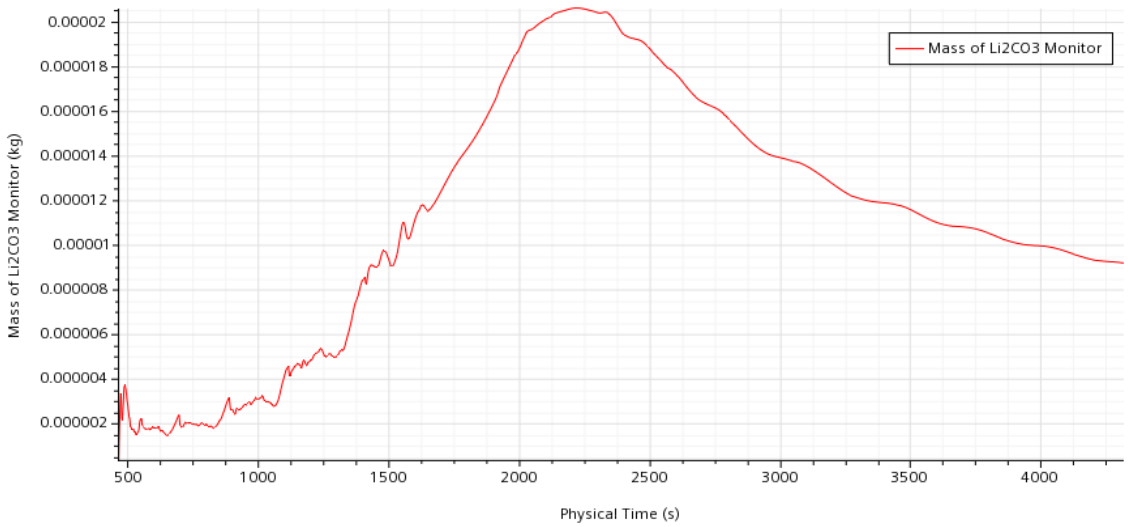

Figure 17: Plot of Li_2CO_3 product formation inside the reactor over time

An indicator for how far Reaction 1 has progressed was tracking the amount of unreacted lithium remaining in the reactor. In Figure 18, the amount of unreacted lithium decreases sharply at first and decreases steadily as the simulation progresses. Towards the end of the reaction, the amount of unreacted lithium begins to asymptote around 0.001 kg, which indicates the first reaction has reached completion.

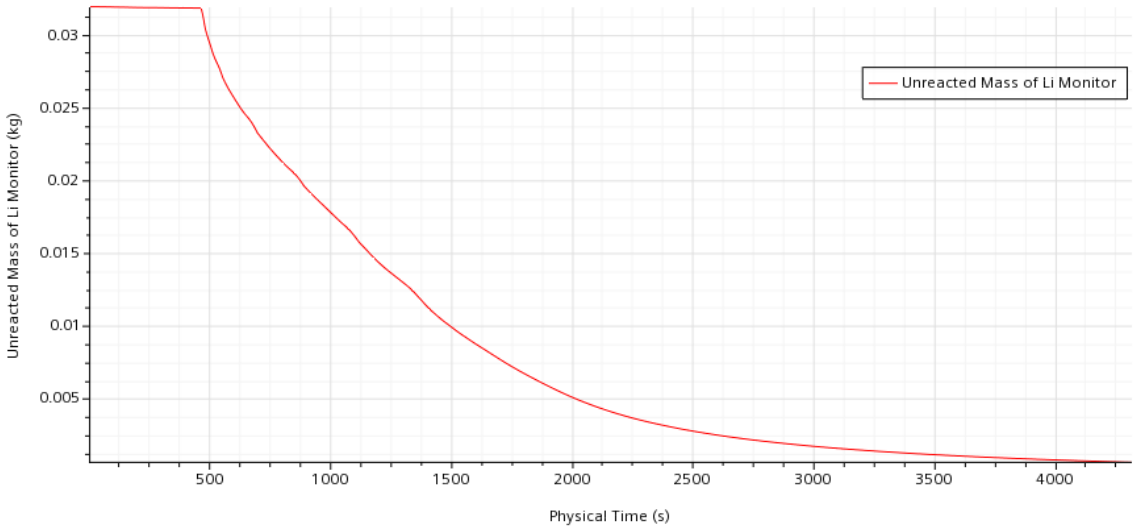

Figure 18: Plot of unreacted lithium over time

It was also important to observe the total amount lithium in the system during the entire simulation to ensure the amount of lithium was being properly conserved. In theory, this number should never change because no lithium is being added to or taken away from the reactor. Rather, the lithium inside the reactor is just being transferred from a reactant to a product. Figure 19 shows the overall mass of lithium in the system.

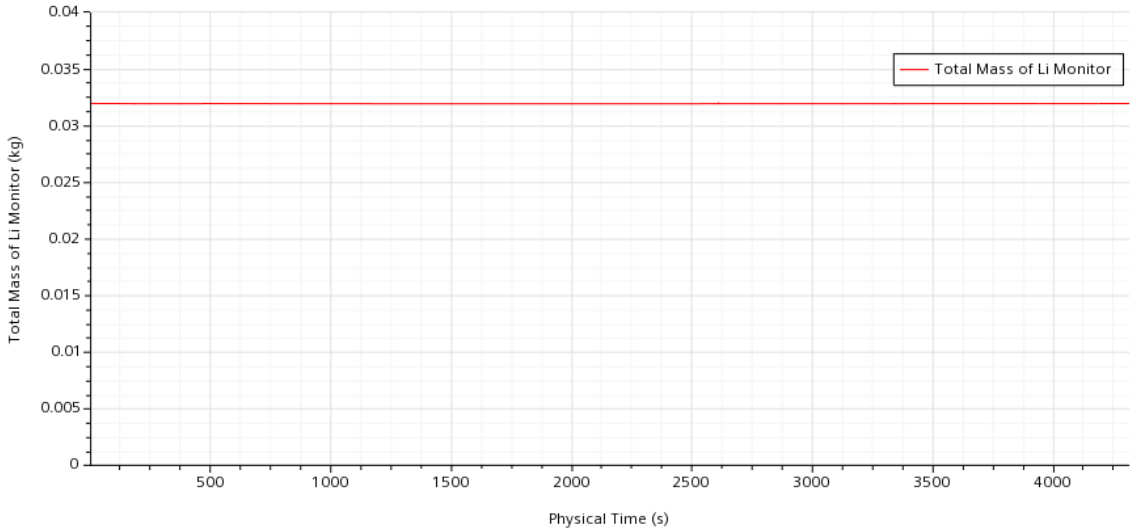

Figure 19: Plot of all lithium mass in the reactor including both reactants and products

Because the trend of the lithium is a flat line, this indicates that the amount of lithium in the reactor is well conserved. In contrast, the mass conservation of carbon and oxygen in Figure 20 was not as well conserved. Even though there are no sudden jumps in the plot, the amount of oxygen (O) and carbon(C) entering the system does not the match the recorded amount of O and C inside the combustor, which indicates a conservation issue. The cumulative mass plots are the amount of C and O entering the reactor through the pressure outlet boundary condition over time and the total mass of C and O plots are the total amount of C and O inside the reactor volume.

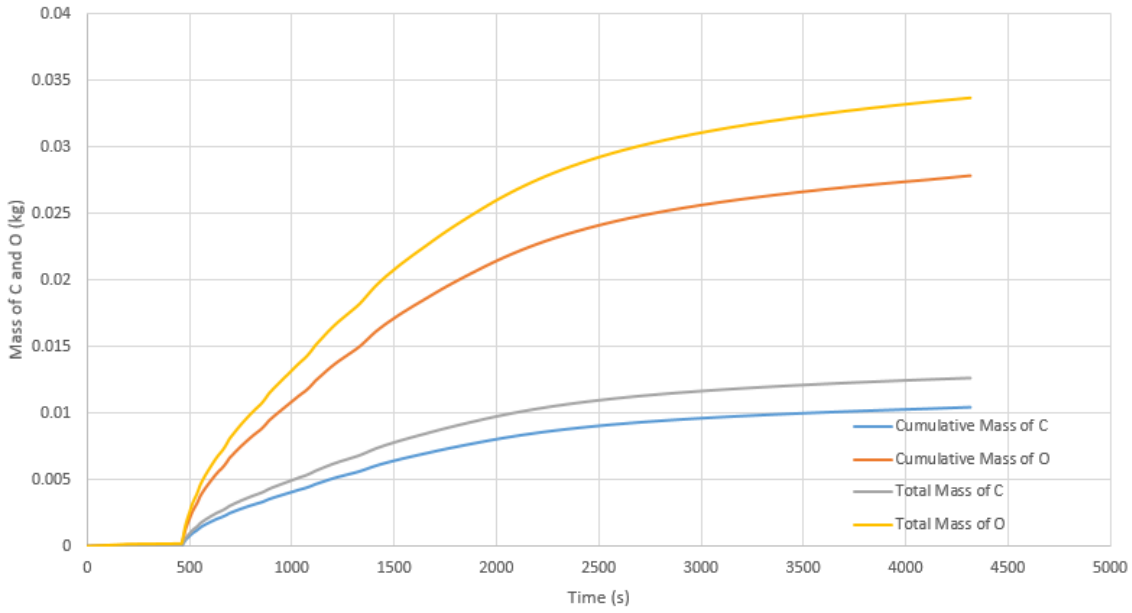

Figure 20: Time integrated and volume integrated masses of carbon and oxygen in the reactor

The trend of the total mass of carbon and oxygen entering the system closely follows the rate at which CO_2 was entering the system in Figure 10. As a result, there is

faster growth occurring in the plot towards the beginning of the reaction, once stabilization ended, and tapers down toward the end of the reaction.

Both sets of figures show the proper ratio of O to C, so the conservation issue may originate in how the integration of the mass flow rate into the combustor was calculated. This issue may have also been exacerbated by a time step that was too large for carbon and oxygen conservation to hold. This conservation issue needs to be explored more fully to discover the cause of this discrepancy.

When comparing the results of the simulation to the results of Reactor 3.2, it is observed that similar results are obtained. The amount of lithium utilization reported in the Reactor 3.2 test [5] was approximately 98% utilization. Comparing that to the simulation results, it is noted that almost all the lithium was consumed by the 1.25-hour mark indicating that similar amounts of lithium were reacted.

The model recorded that 0.004 kg of lithium remained unreacted once the reaction reached completion. Therefore, approximately 99.2% of all lithium in the system was reacted, which is similar to the 98% utilization that Greer et al. [5] recorded. A comparison of the degree of completion between the model and Reactor 3.2 is provided in Table 4.

Table 4: Degree of completion of the model and Reactor 3.2

Reaction	Degree of Completion of Reactor 3.2 (%)	Degree of completion of the Model (%)
Reaction 1	98.5	99.2
Reaction 2	0-25	64.2
Reaction 3 positive	0-9	0

The degree of completion of Reaction 2 in the model was calculated from the total amount of carbon product in the reactor versus the theoretical amount of carbon that would be in the reactor should Reaction 2 have reached 100% completion. It was expected that Reaction 3 positive would show a 0% degree of completion because Reaction 3 negative was continuously disassociating more Li_2CO_3 than what Reaction 3 positive could produce. This occurred because the reactor was hotter than the disassociation temperature of 800°C for the majority of the simulation, meaning more Li_2CO_3 could disassociate than what would be produced from both Reaction 2 and Reaction 3 positive.

The degree of completion values provided by Greer et al. [5] have large error bars in the results. This is due to the difficulty they had in making direct measurements of the degree of completion for each reaction because of the wide variation of products inside the reactor. The degree of completion for Reaction 1 and Reaction 3 of the model compare favorably to Reactor 3.2 results, however, Reaction 2 does not compare as favorably. This is most likely because the parametric fit for Reaction 2 was set too high.

Reducing the rate at which Reaction 2 combusts should lower the overall amount of product formation, which will lower the overall degree of completion.

4.2. Modeling of crust formation

As mentioned above, conditions under which a surface crust might form in the CFD model were explored. To increase the likelihood of crust formation, the temperature of the reactor was brought down to 427 °C, which was even lower than the 700°C bath temperature of Reactor 3.0 as recorded by Greer et al. [5] where they recorded crust formation. Additionally, the target mass flow was decreased by ten percent, and both the mushy-zone permeability model and the slip velocity equations were modified.

The bath temperature was decreased to increase the likelihood of product solidifying at the surface of the lithium bath. It was hoped that any product that was formed would clump together and form a skin over the lithium bath and reduce the rate at which lithium could react with CO_2.

The mass flow rate was reduced to decrease the available CO_2 inside the reactor in order to experiment with attempting to produce a crust. With less CO_2 inside the reactor, the rate of reaction between lithium and CO_2 would decrease which would therefore decrease the overall temperature inside the reactor. With less product forming along with lower temperatures, it was hoped a crust would begin to form on top of the lithium bath.

The mushy-zone permeability model was modified so that the model activated at a lower solid volume fraction of product formation of 0.1 instead of the original value of

0.27. This change was intended to activate the mushy-zone permeability model with less solid product to prevent the small amounts of solid product from sinking beneath the surface of the bath before a critical amount of solid product could be formed. It was theorized that if less solid product was required to form a crust, there would be a higher likelihood of crust formation once more solids were being produced.

The slip velocity equation was further modified to try to prevent CO_2 diffusing through cells that contained over 20% of solid products by volume. This slip velocity equation was modified to:

$$1E-6 * \frac{-\nabla \chi_{CO_2}}{\Delta t} * 5 * \max(0.2 - S_{total}, 0) * \frac{L_{total}}{L_{total} + S_{total} + 1E-5} \quad (30)$$

where χ is the volume fraction of CO_2, Δt is the time step, and L_{total} and S_{total} are the total liquid and solid volume fractions, respectively. These modifications further reduced the slip velocity inside the reactor when more solid product was inside a particular cell. This reduction in slip velocity in cells containing a higher proportion of solid product was intended to further help crust formation by making it less likely the solids would sink to the bottom of the lithium bath and cause less CO_2 availability in cells with a large concentration of solids. However, with these changes, crust formation still did not occur at the free surface of the lithium bath.

To explore the crusting phenomenon in a more isolated manner, the CFD model was simplified to reduce the number of variables that may occlude the actual mechanisms of crust formation. To simplify the model, the mass flow rate was turned off and every reaction was turned off. The lithium bath temperature was set to 700 K and each product was initialized in the reactor as a molten liquid which was placed on top of the molten

lithium bath. Molten reaction products were initialized on top of the molten lithium and then cooled to aid in potential crust formation. The reactor was then cooled, and the formation of solids was analyzed for any indication of crust formation in the reactor.

Solid product formation was observed to have a higher concentration towards the cooling clamp section of the reactor wall and grew outwards towards the center of the reactor, but no crusting occurred on the surface of the reactor. All solid product seemed to form near the cooling clamp, but once solids were formed, the solid product continued to diffuse throughout the molten bath without clumping together. The highest concentration of solid in a cell was recorded at roughly 4.5% at the center of the cooling wall and at the end of the simulation time. The trend of increasing solid volume fraction at the cooling clamp section of the wall is shown in Figure 21.

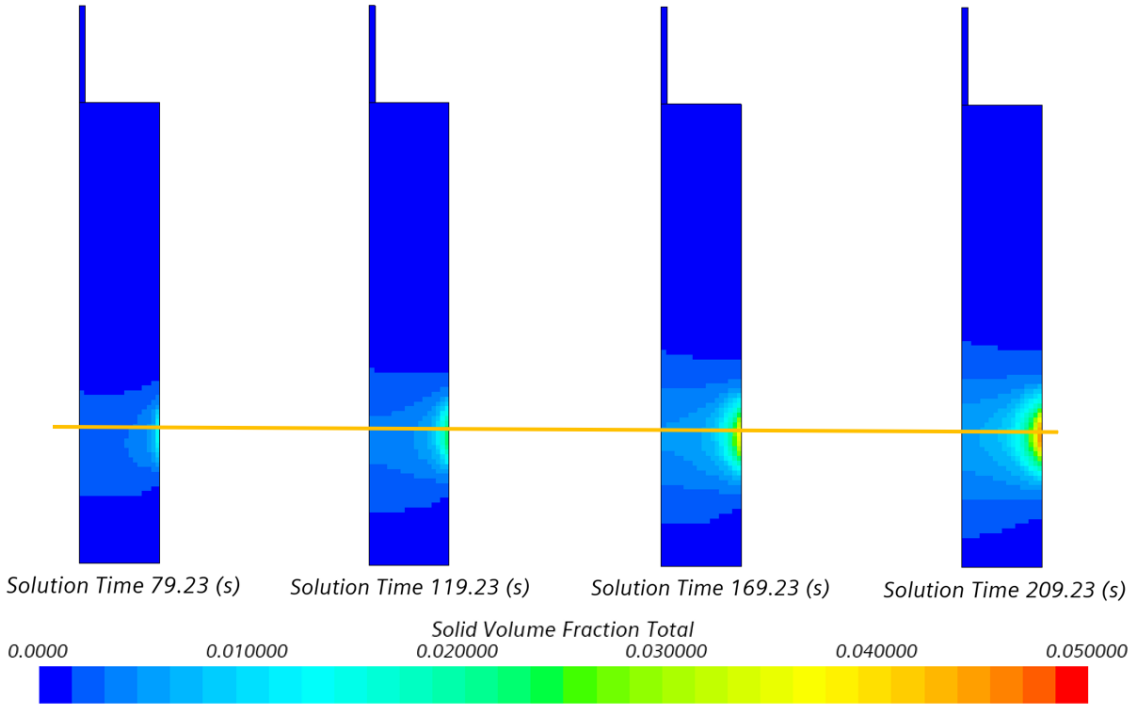

Figure 21: Growth of solid volume fraction in the simplified model without mass flow or reactions enabled. Yellow line indicates surface of lithium bath.

Once it was observed that solid product was forming along the wall of the reactor, the model was re-run from the beginning with the reaction rates and mass flow turned back on, and all products that were initialized on the surface of the lithium bath from the simplified model were removed. The goal of this model was to see if an ongoing reaction would help the formation of a crust due to more products being formed at the free surface. Accordingly, the cooling output of the cooling clamp section of the wall was increased to keep the reactor temperature low to aid in the process of solid product formation. It was found that the solid products behaved as previously noted, and no crust formation occurred inside the reactor.

However, upon continuing this simulation and enabling the melting-solidification flow stop model, a dramatic increase in solid volume fraction near the surface of the lithium bath was observed which indicates a crust may have formed over the lithium bath. This flow stop model stops the flow of solid products above a set threshold value of solid volume fraction. Because there was a limited amount of product in the system, the flow stop model was set to trigger once 8% of a cell contained solid product by volume. This model prevented the solid from sinking to the bottom of the reactor as easily and may have enabled a crust to form. The solid products were prevented from sinking because the flow stop model has stopped the velocity of the solids inside the cell. The solid volume fraction contour plot is provided in Figure 22.

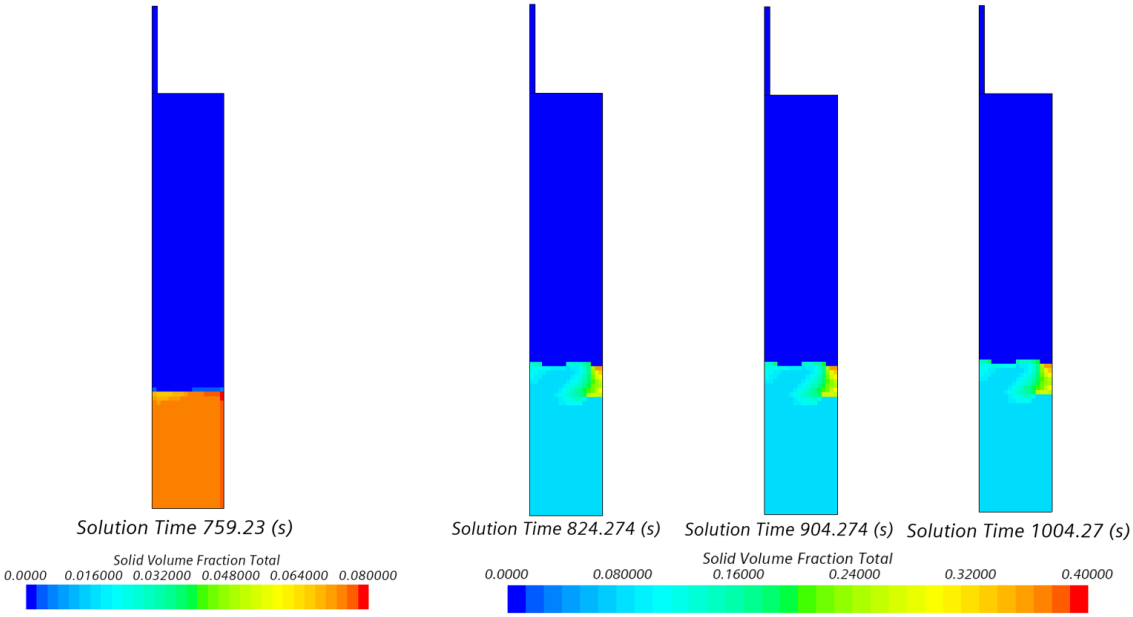

Figure 22: Solid volume fraction in the reactor when the flow stop model was initiated (left) and after the flow stop model has been active for various times.

Before the flow stop model was enabled, the solid products were homogeneously mixed into the lithium bath at a solution time of roughly 760 seconds. Once the flow stop model was enabled, a noticeable crusting began to form at the cooling clamp and spread across the top of the lithium bath. The three contours on the right of Figure 22 show that the model has increased the amount cells that are observing the flow stop model trigger of 8% solid volume fraction or more, which depicts a potential growth of crust formation.

The potential crusting phenomenon was further investigated through analyzing the contours of the lithium volume fraction and a product volume fraction. Figure 23 depicts the lithium volume fraction and Figure 24 depicts the volume fraction of Li_2O.

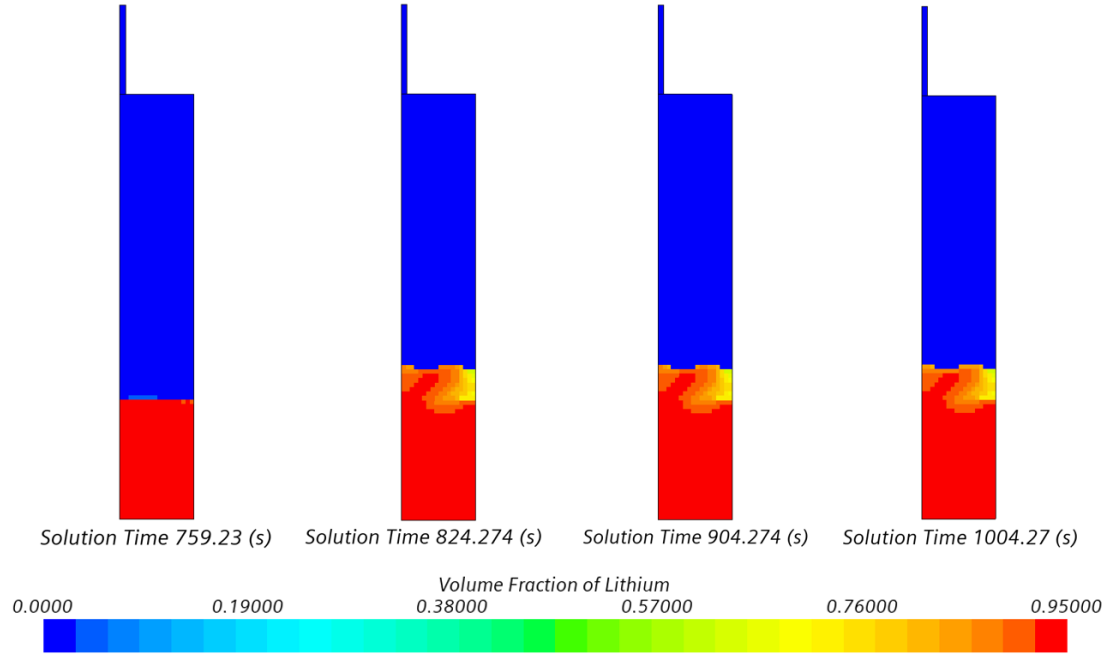

Figure 23: Lithium volume fraction in the reactor when the flow stop model was initiated and after the flow stop model has been active for some time

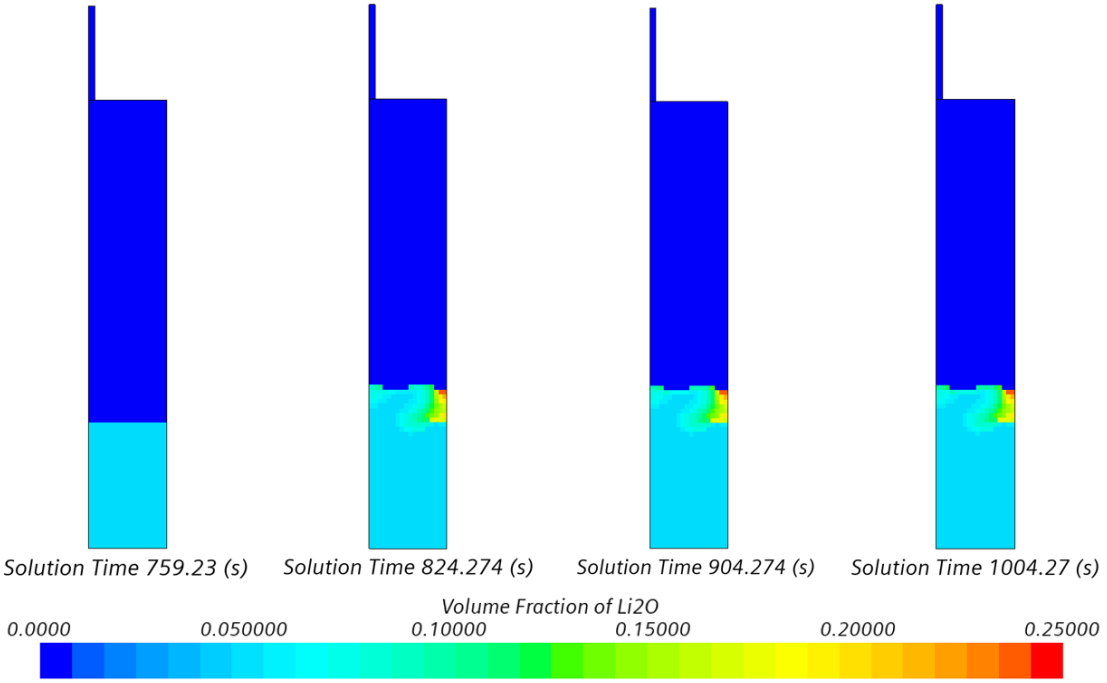

Figure 24: Li_2O volume fraction in the reactor when the flow stop model was initiated and after the flow stop model has been active for some time

As with the solid volume fraction, the reaction products are homogeneously mixed into the lithium bath before the flow stop model is activated. Once the flow stop model was enabled, the products began to form a crust on top of the lithium bath as long as the cell observing the flow stop model had a solid volume fraction at 8% or greater.

As the reaction continued inside the reactor, the concentration of solid product continued to grow towards the center of the reactor until a solid crust began to cut off the surface of the molten lithium from the CO_2 in the headspace. The concentration of solid products is the largest at the cooling wall and begins to diminish in concentration as the crust reaches the center of the reactor.

Although a crust may have potentially formed, the flow stop model may have caused a negative impact to the overall mass conservation of lithium. The error rate of the overall mass of lithium in the reactor increased from nearly 0% to roughly 28%. The mass conservation of lithium for this model is shown in Figure 25.

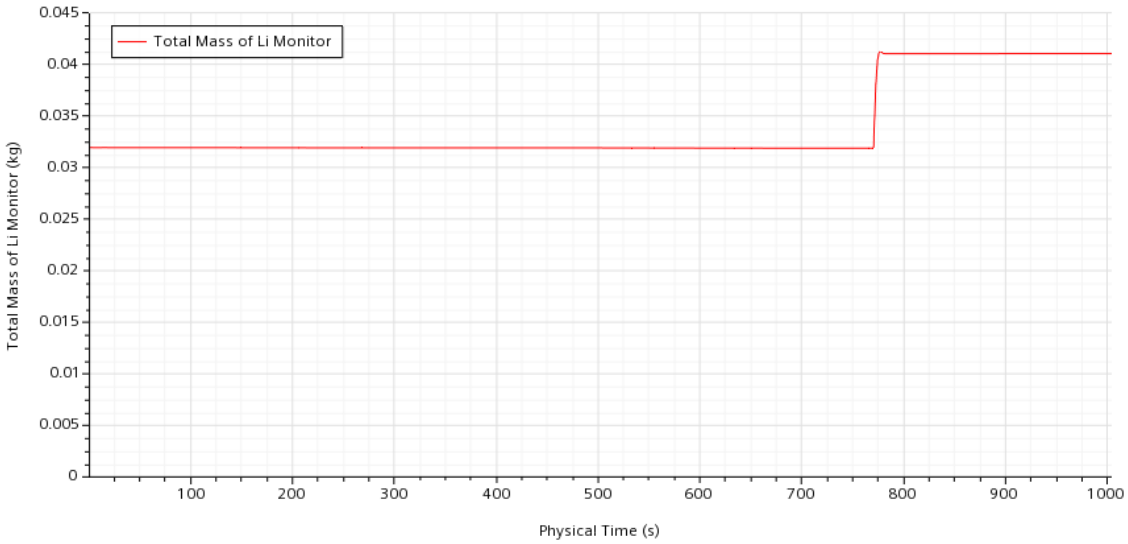

Figure 25: Lithium mass conservation of the model before and after the flow stop model was enabled

This is a very large increase of lithium mass, but this increase may not have impacted the overall crusting phenomenon that was observed. More modeling should probably be conducted to determine if enabling the flow stop model caused this issue and if this issue influenced the overall crusting that was observed.

4.3. Model limitations

This model achieved some limited success in accomplishing a parametric fit of reaction rate constants, where degree of completion of Reaction 1 and Reaction 3 was closely met, but the degree of completion of Reaction 2 was not as closely met, compared to what Reactor 3.2 from Greer et al. [5] reported. Overall, the limited success of the model could be improved further by improving the parametric fit of the reaction rate

constants. A better fit for the reaction rates would provide closer matching data to the experimental tests and further improve overall results.

There is currently limited product interaction occurring within the lithium bath. In the model, only the Li-CO_2, Li_2C_2-CO_2, and Li_2O-CO_2 surface tensions are present. The other surface tensions between CO_2 and lithium carbonate and carbon were not present. Additionally, interaction between products themselves were not included. It is possible that the inclusion of more surface tensions than was used in the simplified model may help create a crust. With more surface tensions, it is possible that more molecules will have a higher likelihood of sticking together more readily due to the cohesive nature of the molecules that are experiencing surface tension. This in turn may create optimal conditions for developing a clump of solid material that could eventually form into a crust of solids at the free surface of the lithium bath. The inclusion of a more complete set of interaction physics may lead to a more accurate portrayal of experimental results. Inclusion of these physics might help in gaining further understanding on how the crust forms and may lead to new discoveries in the prevention of crust formation that can be applied in experiments.

Coinciding with the surface tension limitation, there is a limitation regarding the mesh resolution. The mesh chosen for this model was chosen as a compromise between the accuracy of results and the speed at which the model could run. As a result, the mesh was not as fine as it should probably be. This in turn may have limited the effectiveness of the surface tension models. Surface tension modeling in Star-CCM+ is dependent upon the curvature of the interface, which is how surface tensions are calculated in the momentum equation. Therefore, if the mesh resolution is not fine enough, the interface

may not be captured accurately and will reduce the accuracy of the calculated surface tension forces as a result.

Another limitation of the model is how the model calculates the amount of solid or liquid volume fraction of a product in a particular cell. In reality, lithium oxide, lithium carbide and lithium carbonate each have some amount of miscibility with molten lithium which may prevent some product from precipitating out of solution. This is not accounted for in the model and may have some impact upon how much solid or molten product is available for crust formation. This was addressed to some extent through the inclusion of a drift velocity term which mimicked the miscibility. This limitation could possibly be more fully addressed through using a multi-component liquid phase definition instead of a single liquid phase definition for the combustion products. This phase definition allows for a miscible mixture of two or more pure substances to exist in the same phase, which may provide more physical reactant and product interactions inside the combustor without the need of the drift velocity term. It is believed that this mode of modeling may prove to be more physically realistic.

Chapter 5

Discussion and Conclusions

5.1. Recommended follow-on steps for further development

It is recommended that further development in the model includes more surface tension forces between each product to enhance possible crust formation. For the baseline case and the flow stop model case, only the Li-CO_2, Li_2C_2-CO_2, and Li_2O-CO_2 surface tension interactions are defined. Defining more surface tension forces inside the model will produce product interactions that are more physically sound than current methods. Additionally, it is recommended to reduce the physical time taken to ensure the stability of the model. For the baseline case, around 450 seconds were used before the reaction rates were gradually increased to operating conditions. This time could probably be reduced drastically by reducing the initial under-relaxation factors. This may allow the reaction rates to be increased sooner and more rapidly without the model crashing or producing unphysical results. This should be considered so that downtime is minimized before the simulation reaches a stable state that is ready to accept changes and simulate the reaction. This recommendation will significantly expedite future simulations.

The rates of each reaction should also be investigated further. Currently, the model uses reaction rates that induced CO_2 mass flow rates and product yield similar to those recorded during experimental tests. If the actual reaction rates were known, more precise modeling could be conducted to further match experimental results. Fine-tuning

the reaction rates may also provide some more insights into crust formation though increasing or decreasing the rate at which products can form. It may also be worthwhile to investigate if the reaction of lithium vapor that occurs above the surface [15] has an important role in product and crust formation. Modeling these physics may prove insightful and may lead to a further understanding about how the lithium and products interact during the beginning stages of the reaction.

It would be advantageous to investigate the miscibility of products within the lithium bath and to investigate using multi-component liquid phases instead of single liquid phases. As noted previously, there is some degree of miscibility of the products with the lithium bath. As this was not studied in the current model, a future model should investigate whether miscibility has a role inside the reactor.

An investigation into mesh sensitivity is also warranted. A mesh sensitivity study was not conducted for this model, so it is currently unknown if the results of the model will significantly change from implementing a finer mesh. Therefore, to be confident that the results received are independent of the coarseness of the mesh, a sensitivity test is recommended.

5.2. Overall conclusions

Overall, a CFD model was created that incorporates multi-step chemistry, heat release, heat transfer, conjugate heat transfer, surface tension, drift velocity, and melting-solidification. The CFD model produced an overall lithium fuel utilization similar to Reactor 3.2, achieved a similar average mass flow, and had product yields that were

similar to the experimental test. Additionally, encouraging results were found in modeling the development of a surface crust, similar to what was observed in Reactor 3.0. With the implementation of the flow stop model, it appears that a crust of solid products has formed over the top of the lithium bath. While more testing is needed, the CFD model has shown the potential for crust generation and may provide useful insights into crust formation and prevention in the future. The model developed here is a framework from which further modeling development can proceed. It is hoped that further improvements can be made that will improve the modeling of SCEPS reactors.

These models can be used as a basis for future work aimed at developing a more thoroughly validated model that can aid in the design and development of Li-CO_2 SCEPS reactors. This work, combined with further understanding gained from numerous experimental tests can further advance power generation concepts for planetary landers. These research findings extend our collective knowledge in lithium combustion and this knowledge may increase the efficiencies in combusting lithium and CO_2 inside SCEPS reactors thereby creating a new promising power source in the future.

Bibliography

[1] Glaze, L. S., Wilson, C. F., Zasova, L. V., Nakamura, M., & Limaye, S. (2018). Future of Venus research and exploration. *Space Science Reviews, 214*(5), 1-37. https://doi.org/10.1007/s11214-018-0528-z

[2] Deitrich, N., Insa, L.G., & Bayandor, J. (2021). Venus atmosphere and regolith Earth delivery system. *AIAA Scitech 2021 Forum*. https://doi.org/10.2514/6.2021-0097

[3] Landis, G. A., & Mellott, K. C. (2007). Venus surface power and cooling systems. *Acta Astronautica, 61*(11-12), 995-1001. https://doi.org/10.1016/j.actaastro.2006.12.031

[4] Hunten, D.M., Colin, l., Donahue, T.M., & Moroz, V.I. (1983) *Venus*, The University of Arizona Press, Tuscan, AZ, ISBN 0-8165-0788-0.

[5] Greer, C. J., Peters, J. A., Manahan, M. P., Cor, J. J., & Rattner, A. S. (2021). Experimental characterization of lithium-carbon dioxide combustion in batch reactors for powering Venus landers. *Acta Astronautica, 181*, 235–248. https://doi.org/10.1016/j.actaastro.2021.01.010

[6] Landis, G. A., & Harrison, R. (2010). Batteries for Venus surface operation. *Journal of propulsion and power*, *26*(4), 649-654. https://doi.org/10.2514/1.41886

[7] Landis, G. A., & Haag, E. (2013). Analysis of solar cell efficiency for Venus atmosphere and surface missions. *11th International Energy Conversion Engineering Conference* 4028. https://doi.org/10.2514/6.2013-4028

[8] Mellott, K. (2004). Power conversion with a Stirling cycle for Venus surface mission. *2nd International Energy Conversion Engineering Conference* 5622. https://doi.org/10.2514/6.2004-5622

[9] Cockfield, R. (2000). Radioisotope Stirling generator concepts for planetary missions. *35th Intersociety Energy Conversion Engineering Conference and Exhibit* 2843. https://doi.org/10.2514/6.2000-2843

[10] Board, S. S., & National Research Council. (2012). *Vision and voyages for planetary science in the decade 2013-2022*. National Academies Press. https://doi.org/10.17226/13117

[11] Oleson, S. R. (2018). *COncurrent Multidisciplinary Preliminary Assessment of Space Systems (COMPASS) final report: Advanced Long-life lander Investigating*

the Venus Environment (ALIVE). National Aeronautics and Space Administration, Glenn Research Center. https://ntrs.nasa.gov/citations/20180001292

[12] Miller, T. F., Paul, M. V., & Oleson, S. R. (2016). Combustion-based power source for Venus surface missions. *Acta Astronautica, 127*, 197-208. https://doi.org/10.1016/j.actaastro.2016.05.006

[13] Greer, C. J., Paul, M. V., & Rattner, A. S. (2018). Analysis of lithium-combustion power systems for extreme environment spacecraft. *Acta Astronautica, 151*, 68–79. https://doi.org/10.1016/j.actaastro.2018.05.039

[14] Rhein, R.A. (1990). *Lithium combustion: a review*. NWC – TP – 7087. China Lake CA Naval Weapons Center https://apps.dtic.mil/sti/citations/ADA238154

[15] Yuasa, S., & Isoda, H. (1989). Ignition and combustion of metals in a carbon dioxide stream. *International Symposium on Combustion 22*(1), 1635-1641. https://doi.org/10.1016/S0082-0784(89)80175-4

[16] Rhein, R. A. (1967). *The utilization of powdered metals as fuels in the atmospheres of Venus, Earth, and Mars*. JPL-TR-32-1073, Jet Propulsion Laboratory, California Institute of Technology. http://ntrs.nasa.gov/search.jsp?R=19670010840.

[17] Baker, T., Miller, T. F., Paul, M., & Peters, J. A. (2017). The use of lithium fuel with planetary in situ oxidizers. *10th Symposium on Space Resource Utilization, 2017*. https://doi.org/10.2514/6.2017-0650

[18] Fischer, P., Schiemann, M., Scherer, V., Maas, P., Schmid, G., & Taroata, D. (2015). Experimental characterization of the combustion of single lithium particles with CO2. *Fuel*, *153*, 90–101. https://doi.org/10.1016/j.fuel.2015.02.098

[19] Schiemann, M., Fischer, P., Scherer, V., Schmid, G., & Taroata, D. (2014). Combustion of lithium particles: optical measurement methodology and initial results. *Chemical Engineering & Technology*, *37*(9), 1600-1605. https://doi.org/10.1002/ceat.201400011

[20] Schiemann, M., Bergthorson, J., Fischer, P., Scherer, V., Taroata, D., & Schmid, G. (2016). A review on lithium combustion. *Applied energy*, *162*, 948-965. https://doi.org/10.1016/j.apenergy.2015.10.172

[21] Fischer, P., Schiemann, M., Scherer, V., Maas, P., Schmid, G., & Taroata, D. (2015). A numerical model of the combustion of single lithium particles with CO2. *Fuel*, *160*, 87–99. https://doi.org/10.1016/j.fuel.2015.07.033

[22] Maas, P., Schiemann, M., Scherer, V., Fischer, P., Taroata, D., & Schmid, G. (2018). Lithium as energy carrier: CFD simulations of Li combustion in a 100

MW slag tap furnace. *Applied Energy*, *227*, 506-515. https://doi.org/10.1016/j.apenergy.2017.09.041

[23] Zhou, C. (2013). Numerical simulation on the heat source surface of spray combustion for the fuel of Li/SF6. *51st AIAA Aerospace Sciences Meeting including the New Horizons Forum and Aerospace Exposition* 823. https://doi.org/10.2514/6.2013-823

[24] Siemens (2021) *Simcenter STAR-CCM+* (Version 15.06.008) [Computer software]https://www.plm.automation.siemens.com/global/en/products/simcenter/STAR-CCM.html

[25] Muzaferija, S. (1998). Computation of free surface flows using interface-tracking and interface-capturing methods. *Nonlinear water-wave interaction. Computational Mechanics, Southampton.*

[26] Rodi, W. (1991). Experience with two-layer models combining the k-epsilon model with a one-equation model near the wall. *29th Aerospace sciences meeting*, https://doi.org/10.2514/6.1991-216

[27] Ktalkherman, M. G., Emelkin, V. A., & Pozdnyakov, B. A. (2009). Production of lithium oxide by decomposition lithium carbonate in the flow of a heat carrier. *Theoretical Foundations of Chemical Engineering*, *43*(1), 88-93.

[28] Linstrom, P. J. & Mallard, W. G. *NIST chemistry webbook, NIST standard reference database number 69,* National Institute of Standards and Technology, Gaithersburg MD, 20899, https://doi.org/10.18434/T4D303